# On the effect of the water body geometry on landslide-tsunamis: Physical insight from laboratory tests and 2D to 3D wave parameter transformation

Valentin Heller[1,2,*] and Johannes Spinneken[1]

[1]Department of Civil and Environmental Engineering, Imperial College London, London SW7 2AZ, UK

[2]Geohazards and Earth Processes Research Group, Faculty of Engineering, University of Nottingham, Nottingham NG7 2RD, UK

*Corresponding author: Tel.: +44 1157 484 049.

*E-mail addresses*: Valentin.heller@nottingham.ac.uk (V. Heller), J.spinneken@imperial.ac.uk (J. Spinneken).

**Abstract:** Preliminary landslide-tsunami hazard assessment is commonly based on empirical equations derived from wave channel (2D) or wave basin (3D) experiments. The far-field wave in 2D can easily be an order of magnitude larger than in 3D. The present study systematically investigates the effect of the water body geometry on the wave characteristics in the near- and far-field. Subaerial landslide-tsunami tests were conducted relying upon both a 2D and a 3D physical model, undertaken with identical boundary conditions. The test parameters included two water depths, three rigid slides, as well as various slide release positions. Empirical equations for 3D offshore and laterally onshore wave properties are presented and compared with previous work. A direct comparison of the wave features reveals that the waves decay in 2D, 3D onshore and 3D offshore with $x^{-0.30}$, $r^{-0.67}$ and $r^{-1.0}$, where $x$ (2D) and $r$ (3D) describe the distance from the impact zone. In 2D four wave types are observed, whereas only the two least non-linear types were observed in 3D. This finding is further analysed with wavelet spectra. For a large slide Froude number $\mathsf{F}$, relative slide

thickness $S$ and relative slide mass $M$, the 3D wave heights in the slide impact zone can be as large as in 2D. However, for small $\mathsf{F}$, $S$ and $M$, the 3D waves are considerably smaller both in the near- and far-field. A novel method is presented and validated to transform data from 2D studies to 3D. This method may have favourable implications on preliminary landslide-tsunami hazard assessment.

**Keywords:** Hazard assessment; Impulse wave; Landslide-tsunami; Physical modeling; Water waves; Wave generation.

# 1 Introduction

## 1.1 Overview

Landslide-tsunamis are generated by mass movements such as landslides, slumps, debris flows, rock falls, asteroid impacts, shore instabilities or glacier calving interacting with a water body. They are particularly relevant for regions or mountainous countries such as Austria, Canada, China, Denmark (Greenland), Lesser Antilles (Montserrat), Norway, Spain (Canary Islands), Switzerland or Turkey. Such waves occurred, for instance, in the Lituya Bay, Alaska, in 1958 destroying the forest up to a run-up height of 524 m (Miller, 1960) or in Papua New Guinea in 1998 with 2,100 casualties (Synolakis et al., 2002). If a mass slides into a confined water body such as a reservoir or lake, in similarity to the 1963 Vajont catastrophe with a death toll of about 2,000 (Müller, 1964), the waves are referred to as impulse waves. Many further examples of landslide-tsunamis and impulse waves covered in the reviews of Slingerland and Voight (1979), Huber (1982) and Masson et al. (2006) are a reminder of how frequently such waves occur, and of the considerable risk they may pose for humans and infrastructure. For the remainder of this paper, the terms landslide-tsunamis and impulse waves will be used as interchangeable terms to describe the types of events outlined above.

Landslide-tsunamis need to be reliably predicted on many occasions. Such occasions include the planning and operation phases of reservoirs (Fuchs et al., 2011), or more generally when a slide located above, or partially above, a water body starts to creep such as in the Vajont case (Müller, 1964). Measures to deal with landslide-tsunamis are mainly limited to passive methods such as early warning, evacuation, reinforced infrastructure, safety clearance from ice calving prone areas, reservoir drawdown or provision of adequate freeboard of dam reservoirs. These measures are mainly available for subaerial cases, since mass instabilities are more easily noticed and monitored than for underwater masses. An exact prediction of the wave features is crucial for these passive methods, and such predictions have to be conducted quite frequently during the planning and operational phases of reservoirs, in fiords, lakes or the sea.

Empirical equations developed from generic model studies prove to be popular in dealing with landslide-tsunamis. Generic model studies systematically vary parameters (slide properties, hill slope angle, water depth) which may be estimated a priori for real-world events, and express the unknown wave parameters (amplitude, height, period) as a function of these parameters. The resulting empirical equations can be very efficient in predicting future events (Heller et al., 2009), and are often the most straightforward method if time is limited. At the very least, such equations can help to determine whether or not a prototype specific numerical (Løvholt et al., 2008; Abadie et al., 2012) or physical (Davidson and Whalin, 1974; Fuchs et al., 2011) model study is required. These latter methods are both considerably more expensive and time consuming than applying generic empirical equations.

Generic model studies are conducted under idealised conditions which often concern the slide properties. Perhaps more importantly, idealisations also apply to the geometry of the water body, which is commonly represented by a wave channel (2D) or a wave basin (3D).

Both types of geometries have their justification in real-world applications, and may be considered as two extreme cases of naturally occurring geometries (Heller et al., 2009):

(i) 2D: The slide impacts longitudinally; the slide (subscript s) width $b_s$ being identical or larger than the water body width $b$. The waves are confined as they move along $x$, the longitudinal direction of the water body, without transverse or radial spreading.

(ii) 3D: The slide, with a width $b_s < b$, impacts into a larger water body. The waves propagate laterally and radially from the slide impact zone, and can be described in cylindrical coordinates with the radial distance $r$ and the wave propagation angle $\gamma$.

Tests in 2D are generally more cost efficient, less time consuming and allow better optical access, such that landslide-tsunamis are considerably better investigated and understood in 2D than in 3D. This is reflected in the large number of generic studies investigating subaerial landslide-tsunamis in 2D such as Noda (1970), Wiegel et al. (1970), Kamphuis and Bowering (1972), Slingerland and Voight (1979), Huber and Hager (1997), Monaghan et al. (2003), Walder et al. (2003), Fritz et al. (2004), Quecedo et al. (2004), Liu et al. (2005), Lynett and Liu (2005), Panizzo et al. (2005), Zweifel et al. (2006), Ataie-Ashtiani and Nik-Khah (2008), Heller et al. (2008), Sælevik et al. (2009), Abadie et al. (2010), Heller and Hager (2010, 2011), Fuchs et al. (2013) and Heller and Spinneken (2013). The number of generic studies conducted in 3D is considerably smaller, with Huber and Hager (1997), Liu et al. (2005), Panizzo et al. (2005) and Mohammed and Fritz (2012) as main contributors. Unfortunately, existing 3D studies often exclude the splash zone data, which is considered an important part of the problem for confined water bodies.

## 1.2 Review on the effect of the water body geometry

Chang et al. (1979) investigated experimentally and numerically generated solitary waves in both linear converging and diverging wave channels of side wall angle $\theta = 1.1°$. For relative

distances $x/h < 40$, the wave heights $H_2$ observed at one cross section 2 (subscript 2) is well approximated as a function of $H_1$ at section 1 (subscript 1) with

$$H_2/H_1 = (h_1/h_2)^{1/4}(b_1/b_2)^{1/2}. \tag{1}$$

For constant channel widths $b_1 = b_2$, this latter equation is better known as Green's law, which is based on the concept of energy flux conservation in shallow water of depth $h$. Chang et al. (1979) further observed that, for larger $x/h$ and a diverging channel, the decay is underestimated by Eq. (1) due to viscous damping. Several studies also showed that Eq. (1) has its limitations if applied to solitary or solitary-like waves (Synolakis and Skjelbreia, 1993; Heller et al., 2012).

In investigating tsunamis based on submarine mudslides, Jiang and LeBlond (1994) developed a numerical model using long-wave theory; the fluid being assumed to be inviscid and irrotational. They found that the difference between 2D and 3D depends on the slide width to length ratio $b_s/l_s$. For small $b_s/l_s$, significant differences were found between 2D and 3D. In contrast, for large $b_s/l_s$, the deviations between 2D and 3D were found to be small; this being attributed mainly to the transversal spreading of wave energy in 3D.

Watts et al. (2005) investigated submarine landslide generated tsunamis. In the proximity of the wave generation zone they provide an approximation for the maximum (subscript M) wave amplitude in 3D, $a_{3D,M}$, as a function of the maximum wave amplitude in 2D, $a_{2D,M}$, as

$$a_{3D,M} = a_{2D,M}[b_s/(b_s + L_0)], \tag{2}$$

where $L_0$ is the characteristic wave length. This equation shows that the difference between 2D and 3D is small for a large ratio $b_s/L_0$, whereas the difference may reach an order of

magnitude or more for a small ratio $b_s/L_0$. This is consistent with the findings of Jiang and LeBlond (1994) noted above.

Kranzer and Keller (1959) showed analytically that the wave amplitude decays differently in 2D, with $x^{-1/3}$ to $x^{-1/2}$, compared to 3D, with $r^{-1}$. Similar analytical results are shown by Løvholt et al. (2008). They found a 2D wave height decay ranging from $x^{-1/3}$ (for a monopole-like source) to $x^{-2/3}$ (for a dipole-like source). In 3D, the corresponding wave height decays were found as $r^{-5/6}$ to $r^{-7/6}$. Løvholt et al. (2008) also compared these 3D decays with Boussinesq model simulations of the potential Cumbre Vieja volcano slide at La Palma, establishing a good agreement.

It is important to note that most 2D experimental subaerial landslide-tsunami studies tend to result in smaller wave amplitude or height decays than theoretically predicted. Examples of this are provided by Wiegel et al. (1970) with $a_{2D}(x) \propto x^{-1/5}$, Heller and Hager (2010) with $a_{2D}(x) \propto x^{-4/15}$ or Heller and Spinneken (2013) with $a_{2D}(x) \propto x^{-3/10}$. The experimentally deduced variation is similarly large for 3D studies namely $a_{3D}(r) \propto r^{-19/20}$ in Davidson and Whalin (1974), $H_{3D}(r) \propto r^{-2/3}$ in Huber and Hager (1997), $H_{3D}(r) \propto r^{-0.81}$ in Panizzo et al. (2005) and up to $a_{3D}(r) \propto r^{-1.42}$ in Abadie et al. (2012). The decay may also differ for the primary and secondary wave (Panizzo et al., 2005).

An extensive and systematic comparison of 2D and 3D subaerial landslide generated impulse wave experiments was presented by Huber (1980). The data included approximately 1,000 2D and 150 3D granular slide experiments, which were partially re-analysed by Huber and Hager (1997). The wave height $H$ decays with $x^{-1/4}$ for $x/h \leq 100$ and with $r^{-2/3}$ for $r/h \leq 30$. Huber (1980) states that $H$ between 2D and 3D deviates little from each other near to the slide impact zone such that $H_{3D}(x/h = 5) = H_{2D}(r/h = 5)$ was assumed. Adopting this assumption, Huber and Hager (1997) developed a 3D prediction formula. This formula relies on a 3D data set as well as a generalisation of 2D observations to 3D.

This 2D to 3D transformation method was adopted by Heller et al. (2009) to transform 2D prediction formula for subaerial landslide-tsunamis to 3D and to provide a method to predict their effects including run-up heights, overtopping volumes and forces on dams in reservoirs. Several case studies (e.g. Fuchs and Boes, 2010; Battaglia et al., 2015), showed that the wave features are accurately and efficiently predicted by applying Heller et al. (2009). However, generally speaking, the results appear to lie slightly on the conservative side (over-estimation of wave amplitude and height) in 3D applications.

In seeking to improve the reliability of the method by Heller et al. (2009), Heller et al. (2012) conducted a small scale physical model study. This latter study was conducted with one rigid slide scenario, resulting in a solitary-like wave. The wave was generated in different geometries including 2D, 3D and five intermediate geometries with diverging side walls. Heller et al. (2012) showed that the 2D and 3D wave amplitudes deviate by a factor of 6.7 after a relatively short distance $r/h = 12.5$. The wave height $H_{3D}(r/h = 5)$ is about 20% smaller than $H_{2D}(x/h = 5)$ such that the assumption $H_{3D}(x/h = 5) = H_{2D}(r/h = 5)$ of Huber and Hager (1997) is believed to overestimate the wave height and is conservative for the investigated scenario. Heller et al. (2012) also showed that Eq. (2) results in a rather poor prediction for the investigated case. Eq. (1), on the other hand, resulted in a reasonable prediction of the wave amplitude outside the splash zone for diverging side walls of angles $\theta \leq 30°$, but yielding significant under-predictions for $\theta > 30°$. Due to the small scale adopted by Heller et al. (2012), some results are prone to scale effects. However, they argued that scale effects are likely to cancel out for relative results of data (such as $H_{3D}/H_{2D}$) collected between different small scale models and this statement is investigated in more detail in Section 4.1.2. Irrespective of scale effects cancellation, the general trends observed provide a clear guidance as to the range of test conditions relevant to the present work.

**1.3 Aims of the present study**

Based on the above body of work, the present study aims to:

(i)   Investigate the effect of the water body geometry on the physical characteristics of landslide-tsunamis.

(ii)  Building upon the findings of Heller et al. (2012), significantly extend the range of test cases, thereby investigating different slide width to length ratios $b_s/l_s$, different slide scenarios and the four wave types Stokes-, cnoidal-, solitary- and bore-like waves.

(iii) Establish whether a 2D to 3D transformation of experimental landslide-tsunami data can be undertaken.

(iv)  Advance the understanding of the physical processes that govern landslide-tsunami propagation, and establish how these may differ between 2D and 3D.

To achieve the above aims, the tests are conducted in a medium-scale wave flume (2D) and a medium-scale wave basin (3D); this scale being sufficiently large to exclude the significant scale effects observed in Heller et al. (2012). The 3D data set will consider the most relevant off- and onshore wave features both in the near- (including splash zone) and far-fields. These 3D data will then be directly compared and linked to the 2D results such that a 2D to 3D transformation method can be derived. This novel transformation may make a significant body of work undertaken in 2D accessible for 3D assessments. Additional data analysis using wavelet transforms will also be presented, identifying the key characteristics of wave propagation in 2D and 3D.

The following section introduces the physical models, test programme and measurement systems. The experimental results will first be presented individually for 2D (Section 3.1) and 3D (Section 3.2) before a 2D to 3D transformation method is derived in Section 3.3. The 3D empirical equations are then compared with previous 3D studies in Section 4, along with a

validation of the 2D to 3D transformation method. The most relevant findings are summarised in Section 5.

## 2 Physical models

### 2.1 Overview

It was essential to ensure that the tests in 2D and 3D geometries are conducted under identical boundary conditions and with identical measurement systems. This point is crucial given that model effects (without the effect of the water body geometry) and measurement effects may lead to significant deviations in wave amplitude between different studies (Heller and Spinneken, 2013).

The 2D experiments were conducted in the Coastal Wave Flume and the 3D tests in the Wave Basin of the Hydrodynamics Laboratory of the Department of Civil and Environmental Engineering at Imperial College London. The plan area unobstructed by any beach or wavemaking system was 21 m (length) $\times$ 0.6 m (width) for the flume and 7.4 m $\times$ 20 m for the basin. Fig. 1 shows a photograph of the set-up in the wave basin.

The hill slope ramp shown in Fig. 2 was used throughout, where the slope angle was $\alpha = 45°$ for all tests. It covered the entire channel width in 2D, while it was extended by side walls of up to 7.75 m length in 3D (Fig. 1). These walls were a natural extension of the ramp with identical slope angle $\alpha = 45°$. The front surface of the ramp consisted of PVC sheets. A stainless steel guide in the centre of the ramp surface matched a groove in the slide bottom to ensure that the slide remained in the channel centre during tsunami generation. A pulley system was used to move the slides to the raised positions.

A 1 m long and 2 mm thick rubber sheet, covered with a 2 mm thick stainless steel plate, protected the glass bottom in the immediate slide impact zone in the flume. This rubber sheet and stainless steel plate were also used in the wave basin (Fig. 1). The circular-shaped

transition at the ramp toe was made of a stainless steel sheet bent to an eighth of a circle of radius 0.60 m (Fig. 2). Heller and Spinneken (2013) established that the transition type is a critical test parameter. A radius of 0.60 m was adopted to reduce the sub-pressure effects below the slide when passing the transition, and to provide better consistency between the slide kinematics in 2D and 3D (Section 2.3).

## 2.2 Test programme and parameters

The tsunamis were generated by three rigid slides made of PVC, as shown in the grey box in Fig. 2. A modular slide setup was designed, where the longer slides were constructed as a combination of the shortest slide and a rear extension. As a result, the front face of the slides, including a number of force sensors embedded therein, was identical in all cases. The dynamic bed friction angle between the slide bottom and PVC surface of the ramp was approximately 11°. The masses of the three slides were $m_s$ = 32.51, 60.14 and 82.67 kg and the corresponding densities $\rho_s$ = 1586, 1597 and 1451 kg/m$^3$. This variation in density is due to steel fittings and screws used to hold the PVC sheets together and to connect the slide modules. The slide widths $b_s$ = 0.577 m and thickness $s$ = 0.120 m were constant while the three lengths were $l_s$ = 0.351, 0.599 and 0.878 m (Fig. 2). This resulted in three slide width to length ratios $b_s/l_s$ = 1.64, 0.96 and 0.66.

Fig. 3 shows the medium slide on the slide ramp prior to release. The fittings to connect the rear parts were flush with the slide surface and the electrical cables from the force sensors were run inside the slides and covered with white PVC strips. The hooks to connect the slides to an overhead crane were removed prior to slide release such that the slide surface was flat.

Fig. 2 shows additional relevant slide parameters namely the slide volume $V_s$, the slide front angle $\phi$ and the slide centroid impact velocity $V_s$. Also shown are the hill slope angle $\alpha$ = 45° and still water depth $h$. In 2D the evolution of the wave parameters depends on the

horizontal distance $x$, whereas the radial distance $r$ and the wave propagation angle $\gamma$ are adopted in 3D. In both cases, the coordinate origin is located at the intersection of the slide axis with the water surface and the hill slope face (Fig. 2). The origin for the coordinate along the hill slope $x'$ is defined at the identical location. The most relevant unknown wave parameters are the maximum wave amplitude $a_M$, maximum wave height $H_M$ and maximum wave period $T_M$. The latter is defined as the period of $a_M$ and is found with an up-crossing analysis.

The test programme is shown in Table 1, including the 18 main tests conducted in both 2D and 3D. Six of the 2D tests were repeated twice to confirm the repeatability of the experimental setup. The tests programme was designed to vary the dimensional parameters in wide ranges and to include all four wave types Stokes-, cnoidal-, solitary- and bore-like waves as described in Heller and Hager (2011) and similar wave type classifications (Noda, 1970; Fritz et al., 2004; Zweifel et al., 2006). The test programme included three slides (Fig. 2) and two water depths $h = 0.240$ and $0.480$ m. Given that $h \geq 0.200$ m, scale effects on the primary wave amplitude due to the Reynolds and Weber numbers may be considered negligible (Heller et al., 2008). Each slide was released from 3 different release positions $x'$, resulting in three slide impact velocities $V_s$ (Table 1). For the lowest $V_s$ values the slide nose was located at $x' = 0$ prior to release.

Table 1 also provides the dimensionless parameters, including the slide Froude number $0.54 \leq \mathsf{F} = V_s/(gh)^{1/2} \leq 2.47$ with gravitational acceleration $g$, relative slide thickness $0.25 \leq S = s/h \leq 0.50$, relative slide mass $0.25 \leq M = m_s/(\rho_w b_s h^2) \leq 2.49$ with water (subscript w) density $\rho_w$, and hill slope angle $\alpha = 45°$. These dimensionless parameters result in an impulse product parameter range $0.16 \leq \mathsf{P} = \mathsf{F}S^{1/2}M^{1/4}\{\cos[(6/7)\alpha]\}^{1/2} \leq 1.56$. This parameter $\mathsf{P}$ is related to the streamwise slide momentum flux component and was successfully used to predict 2D wave characteristics in Heller and Hager (2010; 2014).

The three block model parameters introduced by Heller and Spinneken (2013) were constant within this study with relative slide width $b_s/b = 0.96$, slide front angle $\phi = 45°$ and circular-shaped transition. The effect of the water body geometry may also depend on the ratio $0.66 \leq b_s/l_s \leq 1.64$ (Jiang and LeBlond, 1994). However, since $b_s$ is already included in $M$, and $l_s$ is expressed as $l_s \approx V_s/(sb_s)$ for the present block model study, the parameter $b_s/l_s$ is not independent and already considered by $S$ and $M$; this being discussed further in Appendix A.

## 2.3 Measurement system

The present work relies on an extensive test programme which was undertaken in the above noted facilities. This required the acquisition of key physical parameters including surface elevation, pressures on the slide front face, particle image velocimetry (PIV) and slide kinematics. The data analysis and interpretation presented herein focuses on surface elevation and slide kinematics, with slide pressures and PIV data being reported in Heller et al. (2015).

The present data relied on a cable-extension position transducer (Celesco PT5A) to measure the slide kinematics, resistance type wave gauges (Edinburgh Designs WG8) to measure the wave properties and a video camera for optical observations. The position transducer was mounted on the top of the slide ramp and the cable was connected to the rear end of the slides (Fig. 2). Calibrations in both 2D and 3D were conducted several times, and the linearity of the calibration was confirmed. A trigger system ensured that all data was sampled using a common time base.

Fig. 4 shows the position recorded for two tests, and makes a direct comparison between 2D and 3D. The time base was shifted so that at time $t = 0$ the slide nose reaches the still water surface ($x' = 0$). The position measurement follows $x'$ as long as the slide moves parallel to the ramp (until the slide nose reaches the transition). For any subsequent times, the actually

measured distance between the slide rear and the position sensor deviate from the $x'$ coordinate. The slide release positions in 2D and 3D were $x' \approx -1.1$ m. The slide centroid impact velocity $V_s$ was optimised using the slide release position until $V_{s,3D} = V_{s,2D} \pm 5\%$ for two corresponding tests. As a result, the actual release positions may slightly differ between 2D and 3D (Fig. 4).

Observing Fig. 4 further, the slide in 2D is slightly pushed backwards by the primary wave uprush (Section 3.2.1); this being confirmed by video recordings. Such 'negative' velocities were only observed in 2D, only for a limited number of tests, and are of negligible relevance for the primary waves investigated herein. It was generally observed that slides in 3D run-out further than in 2D. This may be due to a small amount of sub-pressure building below the slide when it passes over the transition. This effect is likely to be larger in 2D, due to the limited lateral water supply when compared to 3D. As noted above, the radius of the transition 0.60 m was selected in order to reduce these sub-pressures. This effect is only expected to have a minor influence on the present results. Taken as a whole, the positions and velocities in Fig. 4 are in good agreement during the most important phase of the wave generation process ($t = 0$ - 0.7 s).

The slide velocities shown in Fig. 4 were directly derived from the position through numerical differentiation. The slide reaches its peak velocity shortly after its nose reaches the still water surface. The slide centroid impact velocities $V_s$, occurring when the geometric slide centre reaches the height of the coordinate origin and marked with arrows in Fig. 4, are smaller than the peak velocities for this particular test. The velocities are $V_{s,2D} = 3.14$ m/s and $V_{s,3D} = 3.20$ m/s with a difference of 2%.

The measurement locations of the wave features are shown in Table 2. The wave features were recorded at 128 Hz using resistance type wave probes located at relative distances $x/h = r/h = 3.0, 5.0, 7.5, 10.0, 15.0, 22.5$ and 35.0 in both 2D and 3D with some exceptions for

wave run-up and for $h = 0.480$ m in 3D (Table 2). The wave propagation angles in 3D are $\gamma =$ 0, 15, 30, 45, 58, 73 and 90° (onshore wave run-up). The resistance type onshore wave run-up probes consisted of stainless steel strips bonded to the surface of the side walls (Fig. 1). To maximise the effective basin area, and to minimise any associated wave reflections along the basin side walls, the 3D experimental setup was relocated and rotated for different angles $\gamma$ as appropriate. The set-up in Fig. 1 shows the position adopted to record the wave features at $\gamma =$ 30 and 45°.

## 3 Experimental results

### 3.1 Wave flume (2D)

To adopt the test parameters outlined in Table 1, new 2D experimental data was acquired. The main purpose of this data was to provide a robust base for comparison with the 3D data, following the methodology outlined above. In essence, this new 2D data is expected to be very similar to the data presented in Heller and Spinneken (2013); the only set-up differences being a modification in the ramp transition and slide features. Given that similar data has already been discussed extensively in the past, the discussion of the present 2D data set will be kept very brief. More importantly, the new 2D data will be adopted as a base for comparison within the 3D cases in Sections 3.2 and 3.3.

Fig. 5 shows the maximum wave height $H_M/h$ obtained from the present 2D data. The data representation, including the axes labels and the empirical fitting equation, have been chosen in accordance with Heller and Spinneken (2013). The corresponding empirical equation reads

$$H_M/h = (\mathsf{P}B\varPhi T_\mathrm{s}^{1/4})^{9/10}, \tag{3}$$

14

and good agreement between the present data and this latter equation can be observed (Fig. 5). Within Eq. (3), $\mathsf{P}$ is the impulse product parameter, $B = b_s/b$ considers the blockage ratio, $\Phi = \sin^{1/2}\phi$ expresses the slide front angle $\phi$ and $T_s = t_s/\{[h + \mathcal{V}_s/(sb_s)]/V_s\}$ defines the transition type, with the characteristic time of submerged (subscript s) landslide motion $t_s$. As there is a good fit of this data with the existing 2D empirical equation, no new 2D correlations were derived herein. Additional 2D wave features are discussed in Sections 3.2 and 3.3 as far as they are relevant for the comparison of 2D and 3D wave properties.

## 3.2 Wave basin (3D)

### 3.2.1 Introduction by way of an example

Fig. 6 shows a series of still images of a test in 3D with the set-up in position 2 (measurements at $\gamma = 30$ and 45°). The short slide is in its release position in Fig. 6(a) and the water depth is $h = 0.480$ m. The dimensionless numbers are a slide Froude number $\mathsf{F} = 1.15$, relative slide thickness $S = 0.25$ and relative slide mass $M = 0.25$. The slide impacts into the water body slightly prior to Fig. 6(b) generating an impact crater and a splash which increases in Fig. 6(c). This crater is largest along the slide axis and considerably smaller at $\gamma = 90°$ for the onshore wave run-up. The crater trim collapses in Fig. 6(d), and a highly non-linear wave and an up-rush in the wake of the slide are observed. Fig. 6(d,e) shows the typical semi-circle for primary waves propagating in 3D. The immediate slide impact zone is characterised by air detrainment and a high degree of turbulent flow. The primary wave reaches the first wave probe at $r/h = 3.0$ in Fig. 6(f) followed by the secondary wave, generated by the run-down of the previous up-rush.

Fig. 7(a)-(d) shows the relative water surface elevations $\eta/h$ of the 2D test corresponding to the 3D case shown in Fig. 6. Fig. 7(e)-(h) shows the water surface elevations of the 3D test directly corresponding to the case shown in Fig. 6. The wave profiles along the slide axis are

15

shown for different wave probe locations and plotted versus the relative time $t(g/h)^{1/2}$. The 2D relative primary wave amplitude at the first wave probe is $a_{2D}/h = 0.075/0.480 = 0.16$ [Fig. 7(a)] and the corresponding 3D amplitude is a factor of four smaller with $a_{3D}/h = 0.021/0.480 = 0.04$ [Fig. 7(e)].

In Fig. 7(b) and Fig. 7(e)-(h) the secondary wave is observed to be larger than the primary wave, which is typical only for a small fraction of the conducted tests. In fact, the pattern of the wave group observed shows some features that are characteristic for dispersive wave groups. In the dispersive wave case, a distinct difference between the group velocity and the phase velocity will lead to the apparent transfer of wave energy to the back of the wave group. This energy transfer, in turn, will lead to the leading wave reducing in height, with subsequent waves increasing in magnitude. This effect can clearly be observed in Fig. 7, suggesting that the generated wave indeed forms a dispersive wave group.

The 3D wave decays considerably faster and propagates slower than the 2D wave. In Fig. 7(d) the primary wave amplitude reduces to $a_{2D}/h = 0.028/0.480 = 0.06$ and in Fig. 7(h) to $a_{3D}/h = 0.002/0.480 = 0.004$, resulting in a difference of a factor of 17. Even larger deviations are expected if 2D data are compared with 3D data for $\gamma > 0$, which clearly illustrates the relevance of the effect of the water body geometry.

### 3.2.2 Wave types

Table 3 compares the mean, maxima and minima of the most relevant 2D and 3D primary (subscript 1) wave parameters along the slide axis. On average, 3D waves are more than a factor of two smaller than 2D waves. In contrast, the mean relative wave period $T_1(g/h)^{1/2}$ in 3D is only 21% smaller than in 2D. All 3D waves may be classified as intermediate-water waves ($2 \leq L_1/h \leq 20$), with $L$ as the wave length. Most corresponding 2D waves are also

classified as intermediate-water waves, with a small number of shallow-water cases ($L/h >$ 20).

Heller and Hager (2011) review four approaches to classify landslide-tsunamis namely (i) optical wave profile inspection, (ii) non-linearity $a/H$, (iii) Ursell parameter $\mathsf{U} = (H_1/h)/(h/L_1)^3 = H_1L_1^2/h^3$ and (iv) wavelet transform analysis. All four approaches are applied in the present study and Table 3 includes (ii) and (iii). The criterion $a/H = 0.5$ is a necessary, yet insufficient for a linear wave and $a/H = 1$ is a necessary, yet insufficient for a solitary wave. A more well-defined method to identify the degree of linearity is the Ursell parameter $\mathsf{U}$ (Ursell, 1953). In addition to $a/H = 0.5$, a linear wave also relies on a small relative wave height $H/h$ and steepness $H/L$. Adopting the Ursell parameter, a wave is hence linear for $\mathsf{U} \to 0$. Considering Table 3, the parameter $\mathsf{U}_1$ also confirms that all primary (subscript 1) waves are highly non-linear. It is interesting to observe that 3D waves are less non-linear than 2D waves, according to $\mathsf{U}_1$ in Table 3.

In Fig. 8(a) classification method (i) is applied, where the method of data interpretation and representation is based on Heller and Hager (2011). It is important to note that Heller and Hager (2011) conducted granular slide tests, which may lead to different wave types under identical dimensionless parameters when compared to rigid slides. Fig. 8(a) shows the primary wave types observed in 2D, with the following classification: Stokes-like waves [Fig. 7(b)-(d)] are symmetric relative to both axes, the crest and trough lengths are similarly long, at least two similarly large crests are observed and $a_M < h/2$; cnoidal-like waves are symmetric to the vertical axis, the trough is more pronounced than the crest, at least two crests are observed and $a_M < h$; solitary-like waves are symmetric to the vertical axis and include one dominant crest followed by a very small trough; finally bore-like waves consist of one asymmetric wave crest, the wave front is steep followed by a flat tail, and they transport a

significant amount of air. Examples of tsunami wave profiles for each of the four 2D wave types are presented in Heller and Hager (2011).

The axes in Fig. 8 show the wave type product $\mathsf{T} = S^{1/3}M\cos[(6/7)\alpha]$ versus the Froude number $\mathsf{F}$. Heller and Hager (2011) observed mainly Stokes-like waves in the zone $\mathsf{T} < 4/5\mathsf{F}^{-7/5}$ (dark grey), mainly bore-like waves in the zone $\mathsf{T} > 11\mathsf{F}^{-5/2}$ (white) and mainly cnoidal- and solitary-like waves in the intermediate zone $4/5\mathsf{F}^{-7/5} \leq \mathsf{T} \leq 11\mathsf{F}^{-5/2}$ (light grey). The 18 2D tests of the present study involve all four wave types. However, they are observed in different zones, such that block model tests tend to generate more non-linear wave types at identical $\mathsf{T}$ and $\mathsf{F}$ conditions than granular slides [Fig. 8(a)].

The corresponding 3D primary wave types along the slide axis are shown in Fig. 8(b). These 3D tests involve Stokes- and cnoidal-like waves only, similar to the 3D tests of Panizzo et al. (2005) and Mohammed and Fritz (2012). The lowest zone $\mathsf{T} < 4/5\mathsf{F}^{-7/5}$, originally developed for 2D granular slide tests, remains characteristic for 3D block model tests in the sense that only Stokes-like waves are observed. In the intermediate zone both wave types occur. A general observation is that 3D waves tend more towards the Stokes-like type with increasing distance from the source.

### 3.2.3 Wave parameters

This section addresses the 3D wave parameters and their evolution with $(r/h, \gamma)$. The maximum primary wave parameters are presented in Fig. 9, which includes splash zone data. The figure shows the relative maximum wave amplitude $a_{3D,1,M}/h$ [Fig. 9(a)], wave height $H_{3D,1,M}/h$ [Fig. 9(b)] and the corresponding wave period $T_{3D,1,M}(g/h)^{1/2}$ [Fig. 9(c)]; the abscissae being expressed through the three dimensionless parameters $\mathsf{F}$, $S$ and $M$. The corresponding empirical equations are

$$a_{3D,1,M}/h = 0.50(\mathsf{F}^{1.00}S^{1.10}M^{1.00})^{0.85} \hspace{3cm} (R^2 = 0.96) \hspace{1cm} (4)$$

$$H_{3D,1,M}/h = 0.75(\mathsf{F}^{1.00}S^{1.10}M^{1.00})^{0.70} \hspace{3cm} (R^2 = 0.97) \hspace{1cm} (5)$$

$$T_{3D,1,M}(g/h)^{1/2} = 9(S^{0.40}M^{0.20})^{0.33} \hspace{3cm} (R^2 = 0.50) \hspace{1cm} (6)$$

Eqn. (4) and (5) result in good data fits, given the complexity of the phenomenon, and most data are located within the ±30% bounds. For the maximum wave period shown in Fig. 9(c), no $\mathsf{F}$ dependency was observed, and $\mathsf{F}$ was hence not included on the abscissa. The coefficient of determination $R^2 = 0.50$ for the wave period data is significantly smaller than that observed for the wave amplitude and height. This once again highlights the challenge of expressing the wave period characteristics in a generic way, which may partly be attributed to the mixed occurrence of dispersive and non-dispersive wave forms; further detail being given in Section 3.2.4.

The wave decay characteristics are considered next. The decay term adopted herein is inspired by the study of Huber and Hager (1997), who found $(r/h)^{-2/3}\cos^2(2\gamma/3)$ as a fit to their 3D data. However, both the exponent of the relative distance $r/h$ and the square factor of the cosine were modified due to reasons described hereafter. The overall aim of the decay analysis is to present a uniform wave decay term as a function of $(r/h, \gamma)$ representative for the entire data set. With the present data set involving a variety of dimensionless parameters and wave types, a number of decay descriptions were considered; the following formulation being found to be most suitable:

$$H(r/h, \gamma)/h = f(\mathsf{F}, S, M)(r/h)^{-1.0}f_\gamma \hspace{1cm} \text{with } f_\gamma = \cos^{2\{1 + \exp[-0.2(r/h)]\}}(2\gamma/3). \hspace{1cm} (7)$$

Within this equation, the wave generation and propagation processes are decoupled. The function f($\mathsf{F}$, $S$, $M$) includes the slide impact characteristics and normalises the wave heights.

The waves decay from this normalised level according to the decay term $(r/h)^{-1.0}f_\gamma$. Eq. (7) also applies to the relative wave amplitude $a(r/h, \gamma)/h$, except that a modified normalisation function f($\mathsf{F}$, $S$, $M$) is used.

Fig. 10(a) includes the wave height decay along the slide axis for the three tests encircled in Fig. 8. The curves describing the data start from a level which may be defined by f($\mathsf{F}$, $S$, $M$). The decay $(r/h)^{-1.0}$ results in a good overall approximation of the data. The modification of the decay term for each individual test as a function of the slide impact characteristics, as suggested by Mohammed and Fritz (2012), would not significantly improve the correlation and not justify giving up the simple uniform decay term $(r/h)^{-1.0}$. Note that Fig. 10(a) also includes data from the splash zone, which may alternatively be predicted with Eqn. (4) to (6). The wave height decay $(r/h)^{-1.0}$ is in good agreement with the value $H_{3D} \propto r^{-7/6}$ found in Løvholt et al. (2008) based on a dipole-like source and $a_{3D} \propto r^{-19/20}$ found in the case study Davidson and Whalin (1974). Fig. 10(a) also includes the corresponding 2D tests with wave decay $H_{2D} \propto x^{-0.30}$ (Heller and Spinneken, 2013). The different decay behaviour of 2D and 3D tests is apparent, with 3D tests tending to be smaller and decaying much faster with distance from the source.

Fig. 10(b) shows the relative wave height $H_{3D,1}/h$ versus $\gamma$ and different relative radial distances $(r/h)$ (symbols) for the test with $\mathsf{F} = 0.65$, $S = 0.50$ and $M = 0.98$. Fig. 10(b) also includes the data for the onshore wave run-up at $\gamma = 90°$, which are addressed in detail within Appendix C. Eq. (7) results in a good description of the wave decay, particularly for $r/h \geq$ 10.0. In the near-field, the discrepancy between prediction and measured data seems larger than in the far-field. Those data, including splash data, may separately be predicted with Eqn. (4) to (6) in order to improve the reliability in hazard assessment.

The angle $\gamma$ in the cosine of Eq. (7) was reduced to $2\gamma/3$ after extensive data analysis, reflecting the fact that the wave height at the peripheries $\gamma \to 90°$ is not 0 given that cos(90) =

0. However, it is important to note that this expression is not applicable for the onshore waves (Appendix C). Furthermore, the decay with $\gamma$ in the near-field is larger than in the far-field. This applies to both data within and outside the splash zone; evidence of the latter being provided in Fig. 10(b). This is accounted for in Eq. (7) with the cosine exponent correction term $\{1 + \exp[-0.2(r/h)]\}$. The dashed lines in Fig. 10(b) show the decay if the cosine exponent correction term was absent. The correction term clearly improves the data fit, and this was confirmed during the analysis involving all data.

A multi variable data analysis including all 3D data results in

$$a_{3D,1}(r/h,\ \gamma)/h = 1.75\mathsf{F}^{0.80}S^{1.25}M^{0.67}(r/h)^{-1.0}f_\gamma \qquad\qquad (R^2 = 0.76) \quad (8)$$

$$H_{3D,1}(r/h,\ \gamma)/h = 2.75\mathsf{F}^{0.67}S^{1.00}M^{0.60}(r/h)^{-1.0}f_\gamma \qquad\qquad (R^2 = 0.83) \quad (9)$$

$$T_{3D,1}(r/h,\ \gamma)(g/h)^{1/2} = 5.5M^{0.05}(r/h)^{0.36} \qquad\qquad (R^2 = 0.70) \quad (10)$$

The data fit is shown in Fig. 11, including the relative wave amplitude $a_{3D,1}/h$ [Fig. 11(a)], the relative wave height $H_{3D,1}/h$ [Fig. 11(b)] and the relative wave period $T_{3D,1}(g/h)^{1/2}$ [Fig. 11(c)]. The corresponding coefficient of determinations are $R^2 = 0.76$, $R^2 = 0.83$ and $R^2 = 0.70$, respectively. The symbols in Fig. 11(a,b) specify different wave propagation angles $\gamma$. Only a very small fraction of the data lies outside the $\pm50\%$ bounds, which is considered to be an acceptable fit, particularly since the splash zone data are included. The relative wave period in Fig. 11(c) is reasonably constant with $\gamma$. Furthermore, both the Froude number $\mathsf{F}$ and the relative thickness $S$ are excluded from the correlation in Eq. (10) and Fig. 11(c), as they do not improve the data fit.

The correlations of the 3D data with Eqn. (4) to (6) and (8) to (10) are derived based on the primary wave. In seven out of the 18 3D tests the second wave was larger. These seven tests involve Stokes-like waves which are strongly affected by frequency dispersion which is

further discussed in the next section. Appendix B shows that Eqn. (4), (5), (8) and (9) also result in good first approximations for the maximum wave features, irrespective of their location in the wave train.

### 3.2.4 Wave celerity and frequency dispersion

The wave celerity $c$ is an important parameter to indicate the available time to react to a tsunami after wave generation at a specific distance from the source. The celerity also helps to estimate the wavelength $L$, for example using the regular wave expression $L = Tc$. Fig. 12 shows the relative primary wave celerity $c_1/(gh)^{1/2}$ as a function of the relative mean (subscript m) wave amplitude $a_m/h$ of two subsequent wave probes. The celerity $c$ was derived with the distance between two subsequent wave probes divided by the travel time of the wave crest centre. Within Fig. 12 all 2D and 3D tests are considered, with the celerities of the onshore waves marked in white. Following Kamphuis and Bowering (1972), the data in Fig. 12 are compared with the solitary wave speed approximation given by Boussinesq (1872) as

$$c/(gh)^{1/2} = 1 + a_m/(2h). \qquad (11)$$

Data for $a_m/h > 0.3$ essentially follow Eq. (11), while data at smaller $a_m/h$ are overestimated by the solitary wave speed and follow instead $c_1/(gh)^{1/2} = 1$. This further confirms the observation that a significant number of wave cases, particularly in 3D, may be best described as dispersive wave groups. The celerity of the onshore waves is smaller as they are travelling in reduced effective water depth and are more dispersive. These onshore waves are trapped which significantly affects their propagation behaviour as discussed in detail in Appendix C.

Frequency dispersion and the associated physical processes, such as an apparent energy transfer between successive wave crests, are important because this may (temporarily)

22

enhance trailing waves (Løvholt et al., 2008; Di Risio et al., 2009b). As a consequence, successive wave crests may exceed the primary wave magnitude as was observed in Fig. 7. The effect of frequency dispersion is best investigated using a wavelet transform analysis, providing the energy distribution over the time-frequency domain. In contrast to a Fourier transform, the wavelet transform is not based on periodicity, and is thus suited for the analysis of highly non-stationary tsunamis (Panizzo et al., 2002).

Figs. 13 and 14 show the wavelet spectra based on sym8 for the 2D (a,c) and the corresponding 3D (b,d) tests for the up-most and lower-most encircled tests in Fig. 8. Both Figs. 13 and 14 include two wave probe locations at $x/h = r/h = 3.0$ (a,b) and $x/h = r/h = 15.0$ (c,d). The water surface elevation is shown on the upper part of each subplot. The lower part of each subplot illustrates the corresponding wavelet spectrum by means of contour lines of constant energy density; this energy density being normalised by the maximum energy density occurring for any given case. The time $t$ and frequency $f$ axes are normalised. The wavelet plots also include the solitary wave speed after Eq. (11) in black, with $a_m$ as the mean wave amplitude between two subsequent wave probes, and the dispersive wave celerity in grey. The dispersive wave celerity is computed as $c = \omega/k$, with angular frequency $\omega = 2\pi/T$, wave number $k = 2\pi/L$ and linear frequency dispersion

$$\omega^2 = gk\tanh(kh). \tag{12}$$

At the first wave probe location [Fig. 13(a,b)], the black line indicates the time at which the maximum energy of each frequency component was observed in the vicinity of the primary wave crest. These latter energy maxima are expected to travel with the solitary wave speed for non-dispersive waves, and with a celerity based on linear wave theory for dispersive waves. Fig. 13 includes the 2D bore-like test encircled in Fig. 8 and the corresponding cnoidal-like

wave in 3D; insignificant frequency dispersion being expected for both cases. This is confirmed in Fig. 13(c,d), where the majority of the energy containing frequencies travel at the solitary wave speed. This is indeed one of the tests for which most data show $a_m/h > 0.3$ in Fig. 12, namely for 2D $0.55 \leq a_m/h \leq 1.00$ and for 3D $0.03 \leq a_m/h \leq 0.72$. In marked contrast, Fig. 14 shows the Stokes-like tests encircled in Fig. 8 for 2D and 3D. The black line in Fig. 14(a,b) once again indicates the time of the maximum energy within the first wave crest. In Fig. 14(c,d), further away from the source, the wave energy is clearly seen to travel in close approximation to the linear dispersive wave celerity. This confirms the earlier observations that Stokes-like landslide-tsunamis are in fact highly dispersive (Panizzo et al., 2002). The corresponding data in Fig. 12 are indeed close to the linear dispersive wave speed; this being confirmed for all present 2D and 3D data with $a_m/h \leq 0.13$.

In the context of frequency dispersion, the wavelet spectra reveal potentially distinct behaviour between 2D and 3D. It is expected that 3D waves are more dispersive given that 3D wave periods are on average 21% smaller than the corresponding 2D wave periods (Table 3). For the test in Fig. 13, the energy spectra for the 2D and 3D tests are quite similar, except that the spectral magnitude is smaller in 3D. Small differences are observed for the Stokes-like test in Fig. 14 where the trailing waves exceed the primary wave in 3D. This is reflected in the fact that in seven 3D tests the secondary wave was larger than the primary wave, whereas this was only the case for one test in 2D. It may be concluded that 3D Stokes-like waves are slightly more dispersive than corresponding 2D waves as the former are shorter. In addition, Fig. 14(a,b) shows that the 2D and 3D wave profile shapes are already different close to the source, due to the effect of the water body geometry.

The wavelet transform analysis is also useful in identifying potential wave reflections from the tank side walls. For example, Fig. 13(d) includes some wave energy after relative time 22 (and particularly around 42), which is indicative for wave reflections. However, the associated

energy content is relatively small, and occurs late in the wave train where it is very unlikely to affect the primary wave significantly.

### 3.3 2D to 3D transformation method

Figs. 7, 8 and 10 clearly illustrate that the waves in 2D and 3D differ considerably. While deviations may be relatively small in the slide impact zone, 3D waves decay considerably faster, such that a difference of a factor of 17 can be observed in Fig. 7 after a relatively short propagation distance $x/h = r/h = 22.5$. Fig. 8 reveals that 2D tests show four wave types, while only the two least non-linear types are observed in 3D. Fig. 14 shows that Stokes-like waves in 3D are slightly more dispersive than the corresponding Stokes-like waves in 2D. The present section aims to address all these aspects in a 2D to 3D transformation method; the method being based on a comparison of the primary wave. The primary wave is best suited as its entire wave length is free from significant reflections (Section 3.2.4) and it is propagating in initially still water.

Fig. 15 shows the maximum wave parameters observed in 3D relative to the parameters observed in 2D. This includes the amplitude ratios $a_{3D,1,M}/a_{2D,1,M}$ in Fig. 15(a), the height ratios $H_{3D,1,M}/H_{2D,1,M}$ in Fig. 15(b) and the period ratios $T_{3D,1,M}/T_{2D,1,M}$ in Fig. 15(c). In accordance with our definition of the subscript 1, these parameters refer to the maxima of the primary wave, irrespective of the position of the wave gauge it was recorded. In practice, the 3D maximum wave parameters of the primary wave were always observed at the first wave probe (splash zone) and along the slide axis. In contrast, the maximum wave parameters in 2D were not necessarily observed at the first wave probe. The abscissae in Fig. 15 show the dimensionless slide parameters as before. The wave amplitude and height are described with exponential functions and the corresponding wave period with a linear function as

$$a_{3D,1,M}/a_{2D,1,M} = 1 - \exp(-2.1\mathsf{F}^{0.30}S^{1.00}M^{0.30}) \qquad (R^2 = 0.93) \qquad (13)$$

25

$$H_{3D,1,M}/H_{2D,1,M} = 1 - \exp(-3.5\mathsf{F}^{0.30}S^{1.00}M^{0.30}) \qquad (R^2 = 0.88) \qquad (14)$$

$$T_{3D,1,M}/T_{2D,1,M} = 1.2 - 0.20\mathsf{F} \qquad (R^2 = 0.16) \qquad (15)$$

Eqn. (13) and (14) approach 1 for large $\mathsf{F}$, $S$ and $M$, such that the maximum primary wave amplitudes and heights in 3D approach the corresponding maximum primary wave parameter in 2D for relatively fast, thick and heavy slides impacting into a relatively shallow-water body. Fig. 15(b) includes one point for which $H_{3D,1,M} \approx H_{2D,1,M}$. Another extreme value is $H_{3D,1,M}/H_{2D,1,M} = 0.37$, such that the wave height maximum in 3D is a factor of 2.7 smaller than the corresponding wave in 2D. The wave period ratios $T_{3D,1,M}/T_{2D,1,M}$ tend to decrease with increasing Froude number $\mathsf{F}$. Both dimensionless parameters $S$ and $M$ are not included in Eq. (15) as they do not improve the data fit. The Froude number $\mathsf{F}$ is the dominant parameter for the wave period ratios, while the relative slide thickness $S$ is most important for the wave amplitude and wave height ratios. The dominance of $\mathsf{F}$ in Eq. (15) is interesting, particularly since it is negligible in Eqn. (6) and (10). This behaviour is unclear at present, and remains an open question for future research.

Fig. 16 shows the spatial evolution of the primary wave parameters observed along the slide axis in 3D, relative to the parameters observed in 2D. This includes the primary amplitude ratios $a_{3D,1}(r/h, \gamma = 0°)/a_{2D,1}(x/h)$ in Fig. 16(a), the height ratios $H_{3D,1}(r/h, \gamma = 0°)/H_{2D,1}(x/h)$ in Fig. 16(b) and the corresponding period ratios $T_{3D,1}(r/h, \gamma = 0°)/T_{2D,1}(x/h)$ in Fig. 16(c). Different symbols refer to different slide Froude numbers $\mathsf{F}$. The corresponding empirical equations are

$$a_{3D,1}(r/h, \gamma = 0°)/a_{2D,1}(x/h) = 1.9[(r/h)\mathsf{F}^{-0.40}S^{-0.50}M^{-0.50}]^{-5/6} \qquad (R^2 = 0.92) \qquad (16)$$

$$H_{3D,1}(r/h, \gamma = 0°)/H_{2D,1}(x/h) = 1.8[(r/h)\mathsf{F}^{-0.40}S^{-0.50}M^{-0.50}]^{-2/3} \qquad (R^2 = 0.90) \qquad (17)$$

$$T_{3D,1}(r/h, \gamma = 0°)/T_{2D,1}(x/h) = 0.90 - 0.0035(r/h) \qquad (R^2 = 0.03) \qquad (18)$$

The data in Fig. 16(a,b) shows a good fit, and the vast majority of data points lying within the ±50% bounds. As already observed in Fig. 15(a,b), the differences between 3D and 2D wave parameters vanish for large $F$, $S$ and $M$. Fig. 16 confirms once again the conditions under which 3D waves may be as large as 2D waves in the slide impact zone. However, 3D (along the slide axis) and 2D wave heights differ for small $F$, $S$ and $M$ by up to a factor of 2.7 in the near-field ($r/h = 3.0$) and typically by an order of magnitude in the far-field even within the limit $r/h \leq 35$ of the present study. It is also interesting to observe that the wave amplitude ratios in Fig. 16(a) are lower than the wave height ratios in Fig. 16(b), namely 28% on average over all data. In other words, landslide-tsunamis in 3D show smaller wave amplitude to height ratios than in 2D under otherwise identical conditions. This is consistent with the findings in Fig. 8, where bore- and solitary-like waves in 2D correspond to cnoidal- or Stokes-like waves in 3D. The 3D wave profile is not only smaller but also less non-linear. The wave period ratios $T_{3D,1}/T_{2D,1}$ in Fig. 16(c) start at a value of 0.90 and tend to decrease with relative distance $r/h$. None of the three dimensionless parameters $F$, $S$ and $M$ improve the correlation.

Eqn. (13) to (18) allow for the transformation of 2D wave features to 3D, but only address observations made along the slide axis. The 3D primary wave features for the entire range $r/h \leq 35$ and $0 \leq \gamma \leq 73°$ are described by

$$a_{3D,1}/a_{2D,1} = 1.5[(r/h)F^{-0.40}S^{-0.50}M^{-0.50}]^{-5/6}f_\gamma \qquad\qquad (R^2 = 0.88) \qquad (19)$$

$$H_{3D,1}/H_{2D,1} = 1.5[(r/h)F^{-0.40}S^{-0.50}M^{-0.50}]^{-2/3}f_\gamma \qquad\qquad (R^2 = 0.92) \qquad (20)$$

In comparison to Eqn. (16) and (17), Eqn. (19) and (20) include the additional decay term $f_\gamma$, and the leading factors were modified in order to optimise the data fit. Fig. 17 shows the predicted versus measured data for (a) the relative wave amplitude $a_{3D,1}/h$, (b) the relative

wave height $H_{3D,1}/h$ and (c) the relative wave period $T_{3D,1}(g/h)^{1/2}$. Excellent data fits are observed for the first two graphs and most data lie within the ±50% bounds. Outliers mainly relate to data in the splash zone at $\gamma = 0$ and 15°.

The analysis showed that the wave period is reasonably independent of $\gamma$, which implies that the wave periods along and outside the slide axis are comparable. The correlation in Fig. 17(c), which includes all wave period data, is therefore based on Eq. (18). The transformation method based on Eqn. (13) to (15) and (18) to (20) gives the option to transform 2D wave characteristics to 3D water body geometries, with typically less than ±50% scatter. This method is further validated in Section 4.2.

## 4 Discussion of results

### 4.1 Comparison with previous studies

### 4.1.1 Wave basin (3D)

The findings of four existing 3D studies are described and compared with the present 3D results. The first generic 3D study was conducted by Huber (1980). His tests involved subaerial granular slides impacting in both 2D and 3D water body geometries. The 3D wave basin was 6 m wide and 10 m long and the water depths were $0.12 \leq h \leq 0.36$ m. The granular slide material was dumped behind a flap on a 0.5 m wide hill slope and naturally accelerated down after removal of the flap. The hill slope angle was varied in the range $28 \leq \alpha \leq 60°$. Further dimensionless parameters involved the slide Froude number $1.06 \leq \mathsf{F} \leq 1.84$ (defined with slide front velocity), a relative grain (subscript g) slide volume $0.09 \leq \Psi_g/(b_s h^2) \leq 2.57$ and a relative slide width $1.39 \leq b_s/h \leq 4.17$. Huber and Hager (1997) re-analysed parts of the 3D granular slide experiments of Huber (1980) and included additional data from snow avalanche and glacier calving case studies. Their derived equation, valid for relative radial distances $5 \leq r/h \leq 30$ and wave propagation angles $-90 \leq \gamma \leq 90°$, reads

$$H_{3D,M}/h = 2 \cdot 0.88 \sin\alpha (\rho_s/\rho_w)^{1/4} [\mathcal{V}_s/(b_s h^2)]^{1/2} \cos^2(2\gamma/3)(r/h)^{-2/3}. \tag{21}$$

Panizzo et al. (2005) conducted 3D block model tests. The rigid slides were released into a 12 m long, 6 m wide tank with water depth $h = 0.4$ and 0.8 m. The hill slope angles were $\alpha = 16$, 26 and 36°. The slide was impacting in the corner of the basin and the basin mimicked a quarter of a symmetrical water tank with the side walls as symmetry lines. A spring system at the bottom of the water tank stopped the slide abruptly once it reached the slope toe. The slide density was $\rho_s = 2200$ kg/m$^3$ and the slide front angle $\phi = 90°$. Further parameters were the slide Froude number $1.00 \leq F \leq 2.22$ (with slide front velocity), a dimensionless slide front surface $0.04 \leq sb_s/h^2 \leq 0.68$, relative slide volume $0.02 \leq \mathcal{V}_s/h^3 \leq 0.7$ and dimensionless time of characteristic submerged landslide motion $0.39 \leq t_s(g/h)^{1/2} \leq 5.11$. The last parameter considers the time between slide impact and stop. The wave features were measured with wave probes for relative radial distances $1.3 \leq r/h \leq 15.1$ and wave propagation angles $0 \leq \gamma \leq 90°$. However, splash zone data were excluded in the derivation of the empirical equations. Panizzo et al. (2005) describe the relative primary wave height as

$$H_{3D,1}/h = 0.07[t_s(g/h)^{1/2}]^{-0.30}(Sb_s/h)^{0.88}(\sin\alpha)^{-0.80}\exp(1.37\cos\gamma)(r/h)^{-0.81} \tag{22}$$

with $t_s(g/h)^{1/2} = 0.43(Sb_s/h)^{-0.27}F^{-0.66}(\sin\alpha)^{-1.32}$.

Heller et al. (2009) presented a generic hazard assessment manual including empirical equations for both 2D and 3D landslide-tsunami generation and propagation, as well as run-up on shore lines and dams. The 2D equations were based on the findings later presented in Heller and Hager (2010), and the 3D equations were theoretically deduced with a transformation method implicitly included in Huber and Hager (1997). Huber and Hager (1997) established Eq. (21) to calculate the wave height in 3D. The formula for 2D wave

heights is essentially identical to Eq. (21), except that the 3D decay term $\cos^2(2\gamma/3)(r/h)^{-2/3}$ is replaced by the 2D decay term $(x/h)^{-1/4}$, and the pre-factor 2 is dropped.

The reverse steps were applied by Heller et al. (2009) to transform their 2D equations to 3D, namely the 2D decay term was replaced by $\cos^2(2\gamma/3)(r/h)^{-2/3}$ and a pre-factor 2 was added resulting in

$$H_{3D,M}/h = (3/2)\mathsf{P}^{4/5}\cos^2(2\gamma/3)(r/h)^{-2/3}. \tag{23}$$

The limitations of this equation are $30° \leq \alpha \leq 90°$, $0.86 \leq \mathsf{F} \leq 6.83$ (slide centroid velocity), $0.09 \leq S \leq 1.64$, $0.11 \leq M \leq 10.02$ and $0.59 \leq \rho_s/\rho_w \leq 1.72$, $0 \leq r/h \leq 30$ and $-90 \leq \gamma \leq 90°$. This transformation method must be considered as an engineering approach rather than arising from a highly scientific basis. However, several real-world applications of Heller et al. (2009) confirmed that this transformation method results in realistic predictions (Fuchs and Boes, 2010; Heller and Hager, 2014; Battaglia et al., 2015).

Mohammed and Fritz (2012) conducted a 3D subaerial granular slide study in a 48.8 m long and 26.5 m wide wave basin at water depths of $0.3 \leq h \leq 1.2$ m. The granular material had a grain density of $\rho_g = 2600$ kg/m$^3$ and a slide density of $\rho_s = 1760$ kg/m$^3$. The investigated parameters involved a constant hill slope angle $\alpha = 27.1°$, slide Froude numbers $1 < \mathsf{F} < 4$ (with slide front velocity), relative slide thicknesses $0.1 < S < 0.9$, relative slide widths $1 < b_s/h < 7$, relative slide lengths $2.5 < V_s/(sb_sh) < 6.8$ and relative slide volumes $0.25 < V_s/h^3 < 30$. The wave features were measured for relative radial distances $0 \leq r/h \leq 80$ and wave propagation angles $0 \leq \gamma \leq 90°$. The relative primary wave height is

$$H_{3D,1}/h = 0.31\mathsf{F}^{2.1}S^{0.6}(r/h)^{ex1}\cos\gamma + 0.70\mathsf{F}^{0.96}S^{0.43}[V_s/(sb_sh)]^{-0.50}(r/h)^{ex2}\cos\gamma \tag{24}$$

with $ex1 = -1.2\mathsf{F}^{0.25}S^{-0.02}(b_s/h)^{-0.33}$ and $ex2 = -1.6\mathsf{F}^{-0.41}(b_s/h)^{-0.02}[V_s/(sb_sh)]^{-0.14}$.

Fig. 18 compares the predictions of the four studies above with (a) Eq. (21), (b) Eq. (22), (c) Eq. (23) and (d) Eq. (24); the present 3D data representing the abscissae. Note that the present set of measurements includes splash zone data, with relative wave heights of up to $H_{3D}/h = 1.31$. The data in other 3D studies is limited to $H_{3D}/h < 0.40$ [Eq. (21) from Huber and Hager (1997)], $H_{3D}/h < 0.25$ [Eq. (22) from Panizzo et al. (2005)] and $H_{3D}/h < 0.40$ [Eq. (24) from Mohammed and Fritz (2012)].

Eq. (21) of Huber and Hager (1997) predicts the data of the present study reasonably well [Fig. 18(a)], except for small relative wave heights $H_{3D,1}/h$. This over-prediction for small $H_{3D,1}/h$ is rather surprising given that tests at small water depths $h = 0.12$ m (scale effects) were involved and that granular tests tend to generate smaller waves than block models, at least for a circular transition at the slope toe (Heller and Spinneken, 2013).

Several previous authors also found that Eq. (21) tends to result in rather large wave predictions (Panizzo et al., 2005; Heller and Hager, 2010). The main reason for this overestimation is likely to be the implicit assumption $H_{3D}(x/h = 5) = H_{2D}(r/h = 5)$. In Section 3.3 it was revealed that this assumption may only be applicable at $r/h = 3.0$ and for large $\mathsf{F}$, $S$ and $M$. In Huber (1980) the hill slope, including lateral walls, entered into the wave basin. As a result, the 3D lateral and radial wave propagation in the immediate slide impact zone was restricted (Mohammed and Fritz, 2012). The assumption $H_{3D}(x/h = 5) = H_{2D}(r/h = 5)$ may therefore have been justified in the context of Huber and Hager (1997), but applies considerably less well to the data of the present work. The present study is believed to apply more realistic boundary conditions at the source.

Secondary reasons for the discrepancies observed in Fig. 18(a) are that Eq. (21) is derived for the maximum rather than the primary wave, and that Huber and Hager (1997) defined the Froude number $\mathsf{F}$ with the slide front rather than the slide centroid velocity. The latter point may result in different $\mathsf{F}$ values (Fuchs et al., 2013). Whether this may have an effect on the

data in Fig. 18(a) is difficult to judge, as $V_s$ is not explicitly included in Eq. (21), and is only introduced indirectly in the slope term $\sin\alpha$ (Huber and Hager, 1997).

Eq. (22) from Panizzo et al. (2005) under-predicts the present data by a factor of approximately four [Fig. 18(b)]. In their study the slide abruptly stopped at the slope toe reducing the slide-to-wave energy transformation efficiency (Walder et al., 2003; Heller and Spinneken, 2013). Of secondary relevance for the large discrepancies in Fig. 18(b) may be that Eq. (22) is not designed for the splash zone and that it considers the slide front impact velocity rather than the slide centroid impact velocity. Furthermore, Eq. (22) was applied outside the corresponding slide impact angle limitation of $\alpha \leq 36°$.

Surprisingly, Eq. (23) for the maximum wave height derived by Heller et al. (2009) based on a simple 2D to 3D transformation agrees best with the present data. Nevertheless, it results in an over-estimation of the present data in Fig. 18(c) for $H_{3D}/h \leq 0.50$. The data follow a similar pattern as in Fig. 18(a), since both Eqn. (21) and (23) include an identical decay term. However, the scatter is substantially reduced in Fig. 18(c) compared to Fig. 18(a). Overall, Fig. 18(c) confirms that Eq. (23) provides reasonable predictions which are slightly conservative (over-estimation of the wave height), at least for $H_{3D}/h \leq 0.50$.

Fig. 18(d) illustrates the prediction with Eq. (24) of Mohammed and Fritz (2012). The prediction based on granular slide data under-predicts the present data by a factor of approximately 2.5, which is mainly attributed to the effect of the slide type (Heller and Spinneken, 2013). Furthermore, Eq. (24) is not designed for $H_{3D}/h \geq 0.40$. It is also interesting to observe that the scatter of the present data increases for Eq. (24) when compared to Eqn. (22) and (23). Mohammed and Fritz (2012) included the slide impact characteristics in the exponent of the decay term for $r/h$. This appears to be inadequate for the present rigid slide data, as the scatter increases in Fig. 18(d). This once again underpins the decision to adopt the uniform decay term $(r/h)^{-1.0}$ (Section 3.2.3).

### 4.1.2 2D to 3D transformation

Heller et al. (2012) considered one slide scenario with a slide Froude number $F \approx 1.71$, relative slide thickness $S = 0.50$ and relative slide mass $M = 1.65$ resulting in a solitary-like wave in 2D. The physical model was very small with a water depth $h = 0.10$ m such that the study involved significant scale effects. However, Heller et al. (2012) argued that, even though the dimensional parameters involved significant scale effects, these are likely to cancel out for relative results of data (such as $H_{3D}/H_{2D}$) collected between different small scale models; this assumption being further investigated below.

The present study included a test with $F = 1.51$, $S = 0.50$ and $M = 1.81$. Furthermore, the water depth, channel width and slide thickness were exactly 2.4 times larger than in Heller et al. (2012). Fig. 19 compares the water surface elevations of the new data and the test of Heller et al. (2012) at (a) $x/h = r/h = 3.0$, (b) 5.0 and (c) 10.0. In proximity of the impact zone, the primary wave crest profiles in both 2D and 3D deviate by typically 10-20% [Fig. 19(a)]. These deviations increase with relative distance [Figs. 19(b) and (c)]. The deviations in the primary wave may mainly be attributed to scale effects (Hughes, 1993; Heller et al., 2008), as reflections only occur after the primary wave. The results of Heller et al. (2012) are also included in Figs. 15, 16 and 17, confirming that these dimensionless data of these small scale experiments lies well within the maximum scatter of the data of the present study. This suggests that scale effects indeed mostly cancel out for relative results and that the data by Heller et al. (2012) support the present findings concerning the importance of the water body geometry.

The data of the present study can be compared further to data found with Eq. (2), taken from Watts et al. (2005). This comparison is shown in Fig. 15(a) including two points based on Eq. (2) computed with the test corresponding to the minimum and maximum abscissa value $F^{0.30}S^{1.00}M^{0.30}$. The characteristic wave length $L_0$ was approximated by the measured

wave length at $x/h = r/h = 3.0$, with $L_0 = 3.31$ m (left point) and 3.64 m (right point). A reasonable agreement is achieved for small $\mathsf{F}$, $S$ and $M$ whereas for large $\mathsf{F}$, $S$ and $M$ Eq. (2) underestimates the ratio $a_{3D,1,M}/a_{2D,1,M}$ by a factor of approximately six. Note that Watts et al. (2005) intended to only present an approximation for underwater landslide-tsunamis based on a simple mass balance, and the replacement of $L_0$ with the wave length is a simplification. Nevertheless, the transformation of 2D to 3D results based on Eq. (2) would result in a dangerous underestimation for relatively fast, thick and heavy slides impacting into relatively shallow water.

**4.2 Validation of 2D to 3D transformation method**

This validation of the 2D to 3D transformation method is primarily based on the 2D tests of Heller and Hager (2010). They conducted 211 granular 2D tests in an 11 m long, 0.5 wide and 1 m deep flume. The slide parameters were controlled by means of a pneumatic landslide generator. The investigated dimensionless parameter ranges were $0.86 \leq \mathsf{F} \leq 6.83$, $0.09 \leq S \leq 1.64$, $0.11 \leq M \leq 10.02$ and $30 \leq \alpha \leq 90°$, involving different grain sizes and slide densities heavier and lighter than water. The wave features were measured up to a relative distance of $x/h = 59$.

All normalised wave height data of Heller and Hager (2010) are shown in Fig. 20. The axes representation was chosen in accordance with the present 3D data [Fig. 11(b)] with Eq. (9) also being shown. The transformed 2D data match the present 3D predictions reasonably well with $R^2 = 0.58$, even though the parameter limitations are well exceeded. Approximately 90% of the transformed data lie within the ±50% bounds; this being in close similarity to Fig. 11(b). It is important to stress once again that the non-transformed 2D data would be an order of magnitude too large for 3D water body geometries.

The data in Fig. 20(a) are quite distinct for different slide impact angles $\alpha$. Heller and Hager (2010) found that the wave characteristics change as a function of the impulse product parameter $\mathsf{P}$ including $\{\cos[(6/7)\alpha]\}^{1/2}$, and in the case of the wave height $H \propto \mathsf{P}^{0.80}$. The effect of the slide impact angle $\alpha$ is included for the data in Fig. 20(b) namely with the slide impact angle correction term $f_\alpha^{0.80} = \{\{\cos[(6/7)\alpha]\}^{1/2}/\{\cos[(6/7)45]\}^{1/2}\}^{0.80}$. With $f_\alpha$ the data remain unchanged for $\alpha = 45°$ and adjust for $\alpha \neq 45°$. The data fit improves ($R^2 = 0.71$) in Fig. 20(b) and the data overlap even better than in Fig. 20(a). This is a promising example demonstrating how knowledge gained from 2D studies can be applied to 3D. The 2D to 3D transformation method was further validated for other parameters and also for data from Heller and Spinneken (2013) (not shown herein); the main conclusions supporting the above arguments.

**5 Conclusions**

This study systematically investigated the effect of the water body geometry on subaerial landslide-tsunamis in the near-field (including the splash zone) and far-field. A total of 18 main tests were conducted in a 21 m long and 0.6 m wide wave flume (2D) and repeated in a 7.4 m long and 20 m wide wave basin (3D) under identical boundary conditions. The tests involved two water depths 0.240 and 0.480 m, three slide release positions and three rigid slides with different slide width-to-length ratios. The slide front angles and the hill slope angle were 45°. The wave characteristics are expressed as a function of three dimensionless parameters (i) the slide Froude number $0.54 \leq \mathsf{F} \leq 2.47$, (ii) the relative slide thickness $0.25 \leq S \leq 0.50$ and (iii) the relative slide mass $0.25 \leq M \leq 2.49$. The wave evolution features are expressed as a function of the relative distance $3.0 \leq x/h \leq 35.0$ in 2D and the relative radial distance $3.0 \leq r/h \leq 35.0$ and wave propagation angle $-90 \leq \gamma \leq 90°$ in 3D. Based on the

experimental investigation and an extensive data analysis, the following key conclusions can be drawn:

(I) **Individual conclusions for 2D and 3D**: The 2D wave amplitudes and heights decay with $(x/h)^{-0.30}$. New empirical equations for 3D offshore and lateral onshore waves are presented. The data scatter was found to be relatively small, particularly as the commonly ignored splash-zone data is included. The offshore wave parameters involve the primary wave amplitude, height and period maxima and their evolution with $r/h$ and $\gamma$, where both the wave amplitude and height are described as a function of a uniform decay term $(r/h)^{-1.0}$. The up-crossing wave period depends less on the slide characteristics than the wave amplitude or height. The wave heights are compared with four previous 3D studies; deviations mainly being attributed to different slide models. This comparison further confirms that the wave height in the generic hazard assessment method Heller et al. (2009) is reasonably well predicted. The laterally onshore propagating waves were also analysed (Appendix C). These trapped waves decay slower with $(r/h)^{-0.67}$ than the offshore waves with $(r/h)^{-1.0}$. This reduced decay is mainly attributed to reduced energy spread and the larger dominance of frequency dispersion in an effective reduced water depth. Onshore waves propagate approximately 20% slower than the solitary wave speed. The latter speed describes the offshore waves reasonably well, apart from a number of cases which are better described by linear dispersive wave theory. The maximum wave run-up is typically observed at the second or third wave and it does not further increase with $\mathsf{F}$ and/or $M$ above $\mathsf{F}M > 1.5$.

(II) **3D relative to 2D data**: Four common primary wave types namely bore-, solitary-, cnoidal- and Stokes-like waves are observed in 2D. In contrast, only the two least non-linear types are observed in 3D. This is confirmed by the Ursell parameter showing that the non-linearity is more severe for 2D than for 3D waves. A wavelet analysis reveals that Stokes-like waves are highly dispersive and that dispersion is slightly larger in 3D than in 2D. This is

consistent with the finding that the wave period is on average 21% smaller in 3D. This increased wave dispersion may explain why in some 3D tests the wave maximum was observed later in the wave train than in 2D. Wave heights in the slide impact zone in 3D can be as large as in 2D tests, if $\mathsf{F}$, $S$ and $M$ are large. However, 3D and 2D wave heights along the slide axis differ for small $\mathsf{F}$, $S$ and $M$ by up to a factor of 2.7 in the near-field ($r/h = 3.0$) and typically by an order of magnitude in the far-field within the limit $r/h \leq 35$ of the present study. The wave amplitude to height ratios are consistently smaller in 3D, such that the 3D waves are less non-linear than the 2D waves. A novel method is presented and validated which enables the transformation of 2D wave parameters to 3D resulting in typically less than $\pm50\%$ scatter. This method may have favourable implications on landslide-tsunami hazard assessment given that the knowledge from existing 2D studies may be transformed to 3D.

The presented results aim to support and extend generic hazard assessment methods. More detailed physical insight into selected tests of this study, including forces on the slide surface and wave kinematics, will be presented in Heller et al. (2015).

**Appendix A: Effect of slide width to length ratio**

Jiang and LeBlond (1994) show that the slide width to length ratio $b_s/l_s$ is of relevance to the effect of the water body geometry. Eq. (2) taken from Watts et al. (2005) includes a similar ratio namely the slide width $b_s$ relative to a characteristic wave length $L_0$. In the present study, the ratio $b_s/l_s$ is implicitly considered by two dimensionless parameters (i) the relative slide thickness $S$ and (ii) the relative slide mass $M$ (Section 2.2). Fig. A.1 illustrates the effect of $b_s/l_s$ explicitly through the wave amplitude ratios $a_{3D,1}/a_{2D,1}$ versus the relative distance $x/h$ and $r/h$. Different symbols and colours indicate different $b_s/l_s$ ratios and water depths. Tests conducted at $b_s/l_s = 0.66$ result on average in 28% larger $a_{3D,1}/a_{2D,1}$ ratios than tests conducted at $b_s/l_s = 1.64$. This trend is in agreement with the findings of Jiang and LeBlond (1994). However, considerably more important is the effect of the water depth $h$. Tests conducted at $h = 0.240$ m result on average in 150% larger $a_{3D,1}/a_{2D,1}$ ratios than tests conducted at $h = 0.480$ m. The water depth is included in the denominators of the parameters $\mathsf{F}$, $S$ and $M$, such that the difference between 3D and 2D wave parameters increases with decreasing $\mathsf{F}$, $S$ and $M$ [Eq. (16), Fig. 16(a)]. The data in Fig. 16(a) overlap well compared to the identical data in Fig. A.1 confirming that the effect of $b_s/l_s$ is indeed considered in Fig. 16(a) by $\mathsf{F}$, $S$ and $M$.


**Appendix B: Correlation of 3D maximum wave features**

The correlations for the 3D data represented by Eqn. (4) to (6) and (8) to (10) are derived based on the primary wave. In seven out of the 18 3D tests the second wave was larger. A data correlation analysis was also conducted for the maximum wave, irrespective of its location in the wave train (Table B1). Fig. B.1 shows the maximum relative wave height $H_{3D,M}/h$ [Fig. B.1(a)] and the maximum relative wave height decay $H_{3D,M}(r/h, \gamma)/h$ [Fig. B.1(b)]. The data correlations are based on the same empirical equations as the primary wave, namely Eq. (5) in Fig. B.1(a) and Eq. (9) in Fig. B.1(b). The data scatter only slightly

increases in Fig. B.1 compared to Fig. 9(b) and Fig. 11(b), respectively. The reasons for this small change may be two-fold: (i) only about 40% of the data changes, namely for those seven tests where the primary wave does not include the maximum wave height; (ii) these seven tests are all Stokes-like waves resulting in relatively small waves, only affecting the grey marked area in Fig. B.1(a). Those tests are strongly affected by frequency dispersion as discussed in Section 3.2.4. Table B1 shows the data fit if Eqn. (4) to (6) and (8) to (10) are applied on the maximum wave features. Based on Table B1, Fig. B.1, and further analysis, it is concluded that Eqn. (4), (5), (8) and (9) developed for the primary wave also yield good first approximations for the maximum wave features. However, Eqn. (6) and (10) are a less good approximation for the (maximum) wave period, as the secondary waves are considerably shorter than the primary waves.


**Appendix C: Lateral onshore wave run-up**

In this appendix the laterally onshore propagating waves (trapped waves, edge waves), endangering human lives and infrastructure in proximity of the coast, are investigated. Such onshore wave propagation on a sloping straight coast was investigated by Liu et al. (2005), Lynett and Liu (2005), Di Risio et al. (2009a), Mohammed and Fritz (2012) and Seo and Liu (2013). Di Risio et al. (2009b) and Romano et al. (2013) conducted and analysed tests in a large-scale facility to investigate run-up at a conical island.

These onshore waves were measured while the side wall was 7.75 m (13.4$b_s$) long on the measurement side and about 2 m long on the opposite side (modified compared to Fig. 1). The onshore waves were measured up to $r/h = 22.5$ (Table 2) with stainless steel strips bonded on the wall surface (Fig. 1). The last run-up probe at $r = 5.4$ m was 2.35 m away from the end of the side wall and about 12 m from the end of the basin. Reflections from the offshore

direction affecting the first few waves in the wave train are also not expected since the closest point of the parabolic beach nose was at $r = 6.1$ m in the $\gamma = 0°$ direction.

To allow for a direct comparison of the lateral onshore with the offshore waves, the water depth $h$ was selected as reference length herein. This choice allows for one consistent set of dimensionless parameters throughout the paper, with $h$ being a known parameter prior to tsunami generation. This choice is, however, not based on the physics governing the propagation of the onshore waves. A physically more representative alternative could be based upon a landslide dimension (Lynett and Liu, 2005). Fig. C.1 shows the primary wave run-up (subscript u) $R_{u,1}/h$ decay as a function of the relative distance $r/h$. A multiple variable regression analysis resulted in

$$R_{u,1}/h = 0.25\mathrm{F}^{0.50}S^{0.75}M^{0.50}(r/h)^{-0.67} \qquad\qquad (R^2 = 0.62). \qquad (\mathrm{C}.1)$$

This equation shows that the primary wave run-up decays with $(r/h)^{-0.67}$. This decay lies in between the decay term $(r/h)^{-0.30}$ of the corresponding outwards propagating waves in 2D [Fig. 10(a)] and $(r/h)^{-1.00}$ observed in 3D [Eqn. (8) and (9)]. Limited energy spreading and the larger dominance of frequency dispersion for these in reduced effective water propagating (trapped) onshore waves are likely to be the main reasons why they decay slower than offshore waves. Increased boundary layer effects may be of secondary relevance, as they would contribute to a larger decay.

It may be beneficial to link the onshore with the offshore wave features as the latter are much better understood. The relative primary onshore wave periods are $6.2 \leq T_1(g/h)^{1/2} \leq 21.8$ with a mean of 11.8. This mean is close to 11.4 observed for the offshore waves along the slide axis (Table 3). Furthermore, the onshore primary waves are characterised by relative wave lengths $4.2 \leq L_1/h \leq 18.0$ with a mean of 9.9, non-linearity $0.19 \leq R_{u,1}/(R_{d,1} + R_{u,1}) \leq$

0.81 with a mean of 0.37 and $R_d$ as the run-down (subscript d), and Ursell parameters $1.5 \leq \mathsf{U}_1$ $\leq 37.1$ with a mean of 13.1. This indicates that the onshore waves are slightly less non-linear than the offshore waves (Table 3). The Ursell parameter $\mathsf{U}_1$ would be larger if a reduced water depth rather than $h$ was used.

The wave amplitude along the slide axis $a_{3D,1}(r/h, \gamma = 0°)$ is on average 3.0 times larger than $R_{u,1}$, characterised by a considerable data scatter (not shown herein). A better correlation results when the 3D primary wave amplitude $a_{3D,1}(r/h, \gamma = 73°)$ is related to the primary onshore wave run-up as the former is in close proximity of the side walls. This is shown in the inset in Fig. C.1. The values of $a_{3D,1}(r/h, \gamma = 73°)$ are on average $0.82 R_{u,1}$.

The maximum run-up $R_{u,M}$ may be the most important parameter in an engineering context. Fig. C.2 shows the maximum relative run-up $R_{u,M}/h$ and run-down $R_{d,M}/h$ observed over the entire wave train, versus $\mathsf{F}M$. Highlighted are the relative masses $M$ (colors) and the symbols specify at which wave within the wave train $R_{u,M}$ was observed. Both $R_{u,M}/h$ and $R_{d,M}/h$ tend to increase with $\mathsf{F}$ and $M$ while no dependency on $S$ was observed. The relative maximum run-up $R_{u,M}/h$ is on average 1.51 times larger than the relative maximum run-down $R_{d,M}/h$. Interestingly, $R_{u,M}/h$ was never observed at the primary wave. It was in 14 cases at the second wave, in three cases at the third wave and in one case at the fourth wave measured. Similar observations are described in Lynett and Liu (2005) and Di Risio et al. (2009a;b). The present study further confirms that the maximum onshore wave sometimes increases with $r/h$, reaches a maximum, and then decreases with $r/h$ (Lynett and Liu, 2005; Di Risio et al., 2009a;b). However, for most tests including all at the larger water depth $h = 0.480$ m, the onshore waves already reached their maximum at the first run-up gauge at $r/h = 3.0$.

A regression analysis results in the correlations shown in Fig. C.2 with

$$R_{u,M}/h = 0.15[1 - \exp(-1.5\mathsf{F}M)] \qquad\qquad (R^2 = 0.49) \qquad (C.2)$$

41

$$R_{d,M}/h = -0.10[1 - \exp(-1.5\mathsf{F}M)] \qquad\qquad (R^2 = 0.38) \qquad (\text{C.3})$$

Some valuable trends can be observed in Fig. C.2, despite the rather large data scatter. Firstly, the right hand side of Eq. (C.2) divided by the absolute term on the right hand side of Eq. (C.3) results in 1.50, which is close to the overall mean $R_{u,M}/R_{d,M} = 1.51$ mentioned above. Further, the run-up and run-down tend to be constant relative to $\mathsf{F}$ and $M$ for $\mathsf{F}M > 1.5$. The wave field for $\mathsf{F}M > 1.5$ seems saturated as previously suggested by Di Risio et al. (2009b) for waves propagating around a conical island. For the present study, the saturated relative maximum run-up is $R_{u,M}/h = 0.15$ and the saturated relative maximum run-down $R_{d,M}/h = -0.10$. Furthermore, the location of the maximum run-up was always observed within $r/h \leq 10$, corresponding to $r/b_s \leq 6.2$.

A direct linkage of the maximum onshore run-up waves with the maximum offshore propagating waves has proven to be difficult. This may be because the locations of the maximum offshore waves are in the majority of cases observed at the primary wave (Section 3.2.3), in contrast to the onshore waves which were never observed at the primary wave.

It was shown in Section 3.2.4 that the primary offshore wave, which is in most tests the maximum wave, is not significantly affected by reflections. As the maximum onshore wave run-up typically occurs at the second or third wave within the wave train, potential reflections are once more investigated for onshore waves. In considering wave reflections, the wave celerity is of critical importance. To address this, a wavelet transform is applied to the onshore data set. Fig. C.3 shows the onshore wave run-up at (a) $r/h = 5.0$, (b) 7.5 and (c) 10.0 of the tests previously investigated in Fig. C.1. The last location $r/h = 10$ was selected, as the maximum onshore wave run-up was never observed beyond this location. The onshore wave run-up profiles in Fig. C.3 confirm that the primary wave is considerably smaller than the trailing waves. In considering the wavelet data, some reflected wave energy can be observed

after relative time $t(g/h)^{1/2} = 30$ in Fig. C.3(a). These reflections are likely to result from the parabolic beach in the offshore direction. However, it is very unlikely that these reflections interact significantly with the first three waves. The reflections may interact slightly with the fourth wave, which would only affect one single case in Fig. C.2.

Fig. C.3 further confirms that onshore waves propagate slower than linear waves (Fig. 12). Mohammed and Fritz (2012) and Romano et al. (2013) showed that the wave celerity of edge waves may be approximated with $c = \omega/k$ and the zeroth mode ($n = 0$) of the dispersion relation given by Ursell (1952)

$$\omega^2 = gk_y\sin(2n + 1)\alpha. \tag{C.4}$$

In this equation $\omega$ is the angular wave frequency, $k_y = 2\pi/L$ the wave number of the onshore waves in $y$-direction (subscript y) and $\alpha$ the hill slope angle. Eq. (C.4) characterises the propagation speed of the energy-dominant wave frequencies better than the linear frequency dispersion relation [Eq. (12)].

**Acknowledgment**

**Notation**

$a$ = wave amplitude, m;

$b$ = channel width i.e. water body width, m;

$b_s$ = slide width, m;

$B$ = blockage ratio $B = b_s/b$;

$c$ = wave celerity, m/s;

ex1, ex2 = exponents;

$f$ = wave frequency, 1/s;

$f_\alpha$ = slide impact angle correction term $f_\alpha = \{\cos[(6/7)\alpha]\}^{1/2}/\{\cos[(6/7)45]\}^{1/2}$;

$f_\gamma$ = 3D angle decay function $f_\gamma = \cos^{2\{1 + \exp[-0.2(r/h)]\}}(2\gamma/3)$;

$\mathsf{F}$ = slide Froude number $\mathsf{F} = V_s/(gh)^{1/2}$;

$g$ = gravitational acceleration, m/s$^2$;

$h$ = still water depth, m;

$H$ = wave height, m;

$k$ = wave number, 1/m;

$l_s$ = slide length, m;

$L$ = wave length, m;

$L_0$ = characteristic wave length, m;

$m_s$ = slide mass, kg;

$M$ = relative slide mass $M = m_s/(\rho_w b_s h^2)$;

$n$ = mode;

$\mathsf{P}$ = impulse product parameter $\mathsf{P} = \mathsf{F}S^{1/2}M^{1/4}\{\cos[(6/7)\alpha]\}^{1/2}$;

$r$ = radial distance from the slide impact zone, m;

$R$ = run-up, m;

$R^2$ = coefficient of determination;

| | |
|---|---|
| $s$ | = slide thickness, m; |
| $S$ | = relative slide thickness $S = s/h$; |
| $t$ | = time after slide impact, s; |
| $t_s$ | = characteristic time of submerged landslide motion, s; |
| $T$ | = wave period, s; |
| $\mathsf{T}$ | = wave type product $\mathsf{T} = S^{1/3}M\cos[(6/7)\alpha]$; |
| $T_s$ | = expression considering the transition type $T_s = t_s/\{[h + \mathcal{V}_s/(sb_s)]/V_s\}$; |
| $\mathsf{U}$ | = Ursell parameter $\mathsf{U} = HL^2/h^3$; |
| $V_s$ | = slide centroid impact velocity, m/s; |
| $\mathcal{V}$ | = volume, m$^3$; |
| $x$ | = streamwise distance from the slide impact zone, m; |
| $x'$ | = coordinate along hill slope, m; |
| $z$ | = vertical coordinate, m; |
| $\alpha$ | = slide impact angle i.e. hill slope angle, °; |
| $\phi$ | = slide front angle, °; |
| $\Phi$ | = expression considering the slide front angle $\Phi = \sin^{1/2}\phi$; |
| $\gamma$ | = wave propagation angle, °; |
| $\eta$ | = water surface elevation, m; |
| $\theta$ | = channel side wall angle, °; |
| $\rho$ | = density, kg/m$^3$; and |
| $\omega$ | = angular wave frequency, rad/s. |

Subscript

| | |
|---|---|
| d | = down; |
| g | = grain; |

m   = mean;

M   = maximum;

s   = slide, submerged;

u   = up;

w   = water;

y   = in $y$-direction;

1   = primary; section one; and

2   = section two.


**Abbreviation**

PIV  = particle image velocimetry;

2D  = two-dimensional (wave flume); and

3D  = three-dimensional (wave basin).

**References**

Abadie, S.M., Harris, J.C., Grilli, S.T., Fabre, R., 2012. Numerical modeling of tsunami waves generated by the flank collapse of the Cumbre Vieja Volcano (La Palma, Canary Islands): Tsunami source and near field effects. J. Geophys. Res., 117, C05030.

Abadie, S., Morichon, D., Grilli, S., Glockner, S., 2010. Numerical simulation of waves generated by landslides using a multiple-fluid Navier-Stokes model. Coast. Eng., 57 (9), 779–794.

Ataie-Ashtiani, B., Nik-Khah, A., 2008. Impulsive waves caused by subaerial landslides. Environ. Fluid Mech., 8, 263–280.

Battaglia, D., Strozzi, T., Bezzi, A., 2015. Landslide hazard: risk zonation and impact wave analysis for the Bumbuma Dam – Sierra Leone. Engineering Geology for Society and Territory 2, 1129–1134, G. Lollino, D. Giordan, G.B. Crosta, J. Corominas, R. Azzam, J. Wasowski, N. Sciarra, eds., Springer, Basel.

Boussinesq, J., 1872. Théorie des ondes et des remous que se propagent le long d'un canal rectangulaire horizontal, en communiquant au liquid contenu dans ce canal des vitesses sensiblement pareilles de la surface au fond. J. Math. Pures Appl., 17 (2), 55–108 (in French).

Chang, P., Melville, W.K., Miles, J.W., 1979. On the evolution of a solitary wave in a gradually varying channel. J. Fluid Mech., 95, 401–414.

Davidson, D.D., Whalin, R.W., 1974. Potential landslide-generated water waves, Libby Dam and Lake Koocanusa, Montana. U.S. Army Engineer Waterways Experiment Station. Technical report H-74-15. Corps of Engineers, Vicksburg.

Di Risio, M., Bellotti, G., Panizzo, A., De Girolamo, P., 2009a. Three-dimensional experiments on landslide generated waves at a sloping coast. Coast. Eng., 56 (5-6), 659–671.

Di Risio, M., De Girolamo, P., Bellotti, G., Panizzo, A., Aristodemo, F., Molfetta, M.G., Petrillo, A.F., 2009b. Landslide-generated tsunamis runup at the coast of a conical island: New physical model experiments. J. Geophys. Res., 114 C01009.

Fritz, H.M., Hager, W.H., Minor, H.-E., 2004. Near field characteristics of landslide generated impulse waves. J. Waterw. Port C-ASCE, 130 (6), 287−302.

Fuchs, H., Boes, R., 2010. Berechnung felsrutschinduzierter Impulswellen im Vierwaldstättersee. Wasser Energie Luft, 102 (3), 215−221 (in German).

Fuchs, H., Pfister, M., Boes, R., Perzlmaier, S., Reindl, R., 2011. Impulswellen infolge Lawineneinstoss in den Speicher Kühtai. Wasserwirtschaft, 101 (1-2), 54−60 (in German).

Fuchs, H., Winz, E., Hager, W.H., 2013. Underwater landslide characteristics from 2D laboratory modeling. J. Waterw. Port C-ASCE, 139 (6), 480−488.

Heller, V., Bruggemann, M., Spinneken, J., Rogers, B.D., 2015. Composite modelling of subaerial landslide-tsunamis in different water body geometries and novel insight into slide and wave kinematics (under review).

Heller, V., Hager, W.H., 2010. Impulse product parameter in landslide generated impulse waves. J. Waterw. Port C-ASCE, 136 (3), 145−155.

Heller, V., Hager, W.H., 2011. Wave types of landslide generated impulse waves. Ocean Eng., 38 (4), 630−640.

Heller, V., Hager, W.H., 2014. A universal parameter to predict subaerial landslide-tsunamis? J. Mar. Sci. and Eng., 2 (2), 400−412.

Heller, V., Hager, W.H., Minor, H.-E., 2008. Scale effects in subaerial landslide generated impulse waves. Exp. Fluids, 44, 691−703.

Heller, V., Hager, W.H., Minor, H.-E., 2009. Landslide generated impulse waves in reservoirs - Basics and computation. VAW-Mitteilung 211, R. Boes, ed., ETH Zurich, Zurich.

Heller, V., Moalemi, M., Kinnear, R.D., Adams, R.A., 2012. Geometrical effects on landslide-generated tsunamis. J. Waterw. Port C-ASCE, 138 (4), 286–298.

Heller, V., Spinneken, J., 2013. Improved landslide-tsunami predictions: effects of block model parameters and slide model. J. Geophys. Res., 118 (3), 1489–1507.

Huber, A., 1980. Schwallwellen in Seen als Folge von Felsstürzen. VAW-Mitteilung 180, Vischer, D., ed., ETH Zurich, Zurich (in German).

Huber, A., 1982. Impulse waves in Swiss lakes as a result of rock avalanches and bank slides. Experimental results for the prediction of the characteristic numbers of these waves. Proc., 14th Congrès des Grands Barrages, Rio de Janeiro, ICOLD, Paris, 455–476.

Huber, A., Hager, W.H., 1997. Forecasting impulse waves in reservoirs. Proc., 19th Congrès des Grands Barrages, Florence, ICOLD, Paris, 993–1005.

Hughes, S.A., 1993. Advanced series on ocean engineering 7. Physical models and laboratory techniques in coastal engineering. World Scientific, London.

Jiang, L., LeBlond, P.H., 1994. Three-dimensional modeling of tsunami generation due to a submarine mudslide. J. Phys. Oceanogr., 24 (3), 559–572.

Kamphuis, J.W., Bowering, R.J., 1972. Impulse waves generated by landslides. Proc., 12th Coastal Engineering Conf., Vol. 1, ASCE, New York, 575–588.

Kranzer, H.C., Keller, J.B., 1959. Water waves produced by explosions. J. Appl. Phys., 30 (3), 398–407.

Liu, P.L.-F., Wu, T.-R., Raichlen, F., Synolakis, C.E., Borrero, J.C., 2005. Runup and rundown generated by three-dimensional sliding masses. J. Fluid Mech., 536, 107–144.

Løvholt, F., Pedersen, G., Gisler, G., 2008. Oceanic propagation of a potential tsunami from the La Palma Island. J. Geophys. Res., 113, C09026.

Lynett, P., Liu, L.-F., 2005. A numerical study of the run-up generated by three-dimensional landslides. J. Geophys. Res., 110, C03006.

Masson, D.G., Harbitz, C.B., Wynn, R.B., Pederson, G., Løvholt, F., 2006. Submarine landslides: processes, triggers and hazard prediction. Phil. Trans. R. Soc. A. 364, 2009–2039.

Miller, D.J., 1960. Giant waves in Lituya Bay, Alaska. Geological Survey Professional Paper No. 354-C, U.S. Government Printing Office, Washington, D.C.

Mohammed, F., Fritz, H.M., 2012. Physical modeling of tsunamis generated by three-dimensional deformable granular landslides. J. Geophys. Res., 117, C11015.

Monaghan, J.J., Kos, A., Issa, N., 2003. Fluid motion generated by impact. J. Waterw. Port C-ASCE, 129 (6), 250–259.

Müller, L., 1964. The rock slide in the Vajont Valley. Rock Mech. Eng. Geol., 2 (3-4), 148–212.

Noda, E., 1970. Water waves generated by landslides. J. Waterway. Harbour. Coast. Eng. Div. ASCE, 96 (WW4), 835–855.

Panizzo, A., Bellotti, G., De Girolamo, P., 2002. Application of wavelet transform analysis to landslide generated waves. Coast. Eng., 44 (4), 321−338.

Panizzo, A., De Girolamo, P., Petaccia, A., 2005. Forecasting impulse waves generated by subaerial landslides. J. Geophys. Res., 110 C12025.

Quecedo, M., Pastor, M., Herreros, M.I., 2004. Numerical modeling of impulse wave generated by fast landslides. Int. J. Numer. Methods Eng., 59, 1633–1656.

Romano, A., Bellotti, G., Di Risio, M., 2013. Wavenumber-frequency analysis of the landslide-generated tsunamis at a conical island. Coast. Eng., 81 (11), 32–43.

Sælevik, G., Jensen, A., Pedersen, G., 2009. Experimental investigation of impact generated tsunami; related to a potential rock slide, Western Norway. Coast. Eng., 56 (9), 897–906.

Seo, S.N., Liu, P. L.-F., 2013. Edge waves generated by landslides on a sloping beach. Coast. Eng., 73 (3), 133–150.

Slingerland, R.L., Voight, B., 1979. Occurrences, properties and predictive models of landslide-generated impulse waves. Rockslides and avalanches, Vol. 2, B. Voight, ed., Elsevier, Amsterdam, 317–397.

Synolakis, C.E., Bardet, J.-P., Borrero, J.C., Davies, H.L., Okal, E.A., Silver, E.A., Sweet, S., Tappin, D.R., 2002. The slump origin of the 1998 Papua New Guinea tsunami. Proc. R. Soc. Lond. A, 458, 763–789.

Synolakis, C.E., Skjelbreia, J.E. 1993. Evolution of maximum amplitude of solitary waves on plane beaches. J. Waterw., Port, Coastal, Ocean Eng., 119 (3), 323–342.

Ursell, F., 1952. Edge waves on a sloping beach. Proc. R. Soc. Lond. A, 214, 79–97.

Ursell, F., 1953. The long-wave paradox in the theory of gravity waves. Math. Proc. Cambridge, 49, 685–694.

Walder, J.S., Watts, P., Sorensen, O.E., Janssen, K., 2003. Tsunamis generated by subaerial mass flows. J. Geophys. Res., 108 (B5), 2236(2).

Watts, P., Grilli, S.T., Tappin, D.R., Fryer, G.J., 2005. Tsunami generation by submarine mass failure. II: Predictive equations and case studies. J. Waterw., Port, Coastal, Ocean Eng., 131 (6), 298–310.

Wiegel, R.L., Noda, E.K., Kuba, E.M., Gee, D.M., Tornberg, G.F., 1970. Water waves generated by landslides in reservoirs. J. Waterway. Harbour. Coast. Eng. Div. ASCE, 96 (WW2), 307–333.

Zweifel, A., Hager, W.H., Minor, H.-E., 2006. Plane impulse waves in reservoirs. J. Waterw. Port C-ASCE, 132 (5), 358–368.

**Table 1.** Test programme with dimensional and dimensionless parameters in 2D: all slide parameters are identical in 3D except for the slide velocity which may vary by up to ±5%; tests with * were three times conducted in 2D to investigate the repeatability.

| Slide type | $h$ (m) | $V_s$ (m/s) | $s$ (m) | $m_s$ (kg) | $b_s$ (m) | F (-) | S (-) | M (-) |
|---|---|---|---|---|---|---|---|---|
| Short slide | 0.240 | 0.94*, 2.54, 3.79 | 0.120 | 32.51 | 0.577 | 0.61, 1.66, 2.47 | 0.50 | 0.98 |
| | 0.480 | 1.16*, 2.38, 3.12 | 0.120 | 32.51 | 0.577 | 0.54, 1.10, 1.44 | 0.25 | 0.25 |
| Medium slide | 0.240 | 1.21*, 2.32, 3.14 | 0.120 | 60.14 | 0.577 | 0.79, 1.51, 2.05 | 0.50 | 1.81 |
| | 0.480 | 1.47*, 2.45, 3.21 | 0.120 | 60.14 | 0.577 | 0.68, 1.13, 1.48 | 0.25 | 0.45 |
| Long slide | 0.240 | 1.37*, 2.17, 2.78* | 0.120 | 82.67 | 0.577 | 0.89, 1.42, 1.81 | 0.50 | 2.49 |
| | 0.480 | 1.89, 2.53, 3.01 | 0.120 | 82.67 | 0.577 | 0.87, 1.17, 1.39 | 0.25 | 0.62 |

**Table 2.** Wave probe locations: 7 measurement locations in 2D for both water depths were covered, 48 locations in 3D for $h$ = 0.240 m and 40 locations for $h$ = 0.480 m; note that the entire data set in 3D was collected with three different ramp positions in the wave basin.

| Geometry | Water depth $h$ (m) | Wave propagation angle $\gamma$ (°) | Relative distance $x/h$ or $r/h$ (-) |
|---|---|---|---|
| 2D | 0.240, 0.480 | 0 | 3.0, 5.0, 7.5, 10.0, 15.0, 22.5, 35.0 |
| 3D | 0.240 | 0, 15, 30, 45, 58, 73 | 3.0, 5.0, 7.5, 10.0, 15.0, 22.5, 35.0 |
| 3D | 0.480 | 0, 15, 30, 45, 58, 73 | 3.0, 5.0, 7.5, 10.0, 15.0, 22.5 |
| 3D | 0.240 | 90 (onshore wave run-up) | 3.0, 5.0, 7.5, 10.0, 15.0, 22.5 |
| 3D | 0.480 | 90 (onshore wave run-up) | 3.0, 5.0, 7.5, 10.0 |

**Table 3.** Comparison of 2D and 3D primary wave features based on the 3D parameters along the slide axis.

| Parameter | Geometry | $a_1/h$ | $H_1/h$ | $T_1(g/h)^{1/2}$ | $L_1/h$ | $a_1/H_1$ | $U_1$ |
|---|---|---|---|---|---|---|---|
| Mean | 2D | 0.360 | 0.466 | 14.4 | 16.4 | 0.71 | 182.0 |
| | 3D | 0.134 | 0.222 | 11.4 | 11.8 | 0.47 | 33.4 |
| | 3D to 2D parameter (%) | 37 | 48 | 79 | 72 | 66 | 18 |
| Maximum | 2D | 1.225 | 1.570 | 31.3 | 38.9 | 0.98 | 1029.0 |
| | 3D | 1.020 | 1.312 | 18.1 | 18.3 | 0.95 | 315.9 |
| Minimum | 2D | 0.041 | 0.076 | 6.1 | 6.2 | 0.46 | 8.6 |
| | 3D | 0.003 | 0.007 | 5.5 | 5.9 | 0.26 | 0.5 |

**Table B1.** Quantification of data fit of 3D data: coefficients of determination $R^2$ of maximum wave features described with equations derived for the primary wave features.

| Equation (wave parameter) | Primary wave | Maximum wave |
|---|---|---|
| Eq. (4) ($a_{3D,1,M}$) | $R^2 = 0.96$ [Fig. 9(a)] | $R^2 = 0.95$ |
| Eq. (5) ($H_{3D,1,M}$) | $R^2 = 0.97$ [Fig. 9(b)] | $R^2 = 0.96$ [Fig. B.1(a)] |
| Eq. (6) ($T_{3D,1,M}$) | $R^2 = 0.50$ [Fig. 9(c)] | $R^2 = 0.22$ |
| Eq. (8) [$a_1(r/h, \gamma)$] | $R^2 = 0.76$ [Fig. 11(a)] | $R^2 = 0.63$ |
| Eq. (9) [$H_1(r/h, \gamma)$] | $R^2 = 0.83$ [Fig. 11(b)] | $R^2 = 0.78$ [Fig. B.1(b)] |
| Eq. (10) [$T_1(r/h, \gamma)$] | $R^2 = 0.70$ [Fig. 11(c)] | $R^2 = 0.15$ |



**Fig. 1.** Wave basin set-up in position 2 showing on the left: medium slide on ramp, circular transition and steel plate on ramp toe and side-walls with run-up gauges; centre: first wave probes at $r/h = 3.0$, $5.0$, $7.5$ and $10.0$ for $\gamma = 30º$ and $45º$ and $h = 0.480$ m; right: bridge supporting the beams hosting the wave probes and tripod for video recordings; note that the set-up was relocated for the measurements at $\gamma = 0º$, $15º$ (position 1) and at $58º$, $73º$ and $90º$ (position 3) and the side walls were extended in position 3.
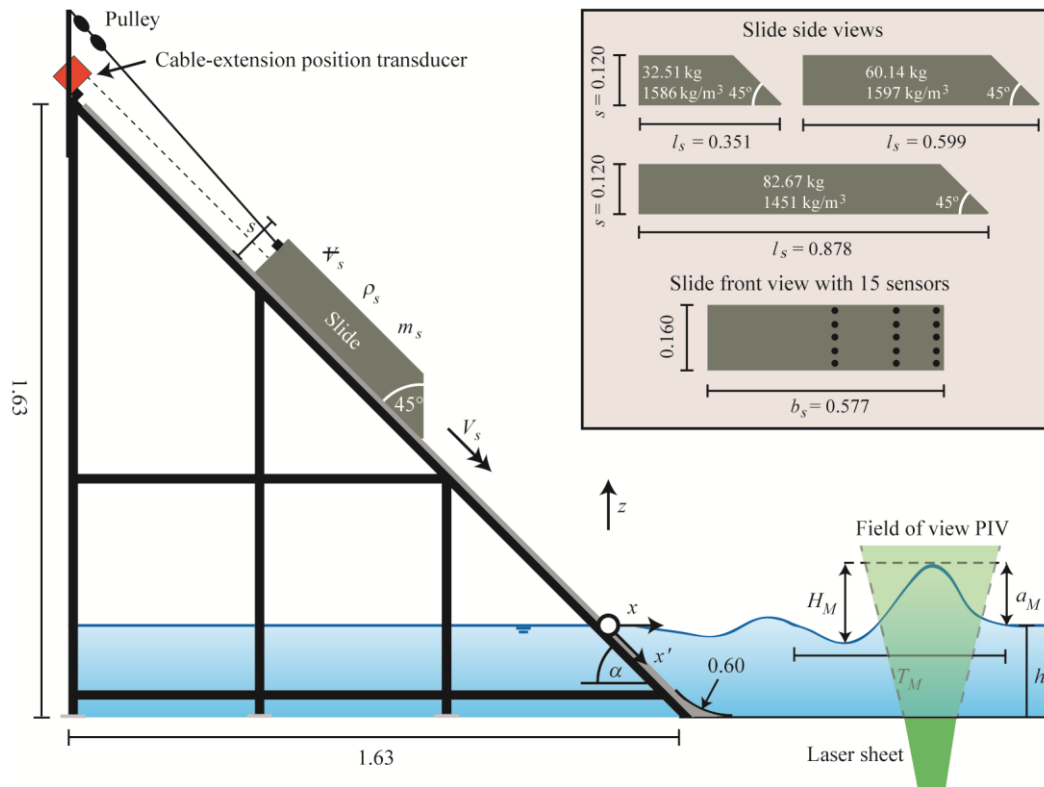
**Fig. 2.** Side view of landslide-tsunami set-up and measurement system including the slide properties in the grey box; all length dimensions are in m.
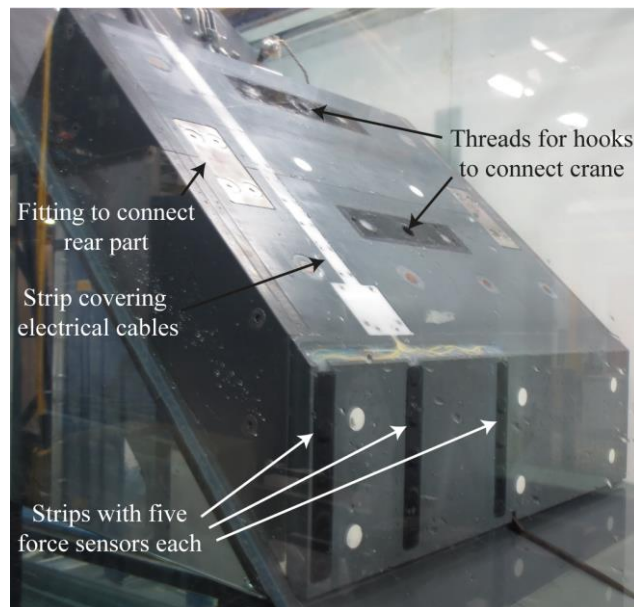


**Fig. 3.** Medium slide in release position in 2D: slide front with 15 force sensors, white PVC strip to cover electrical cables, fittings to connect rear part and threads for the hooks to connect the overhead crane.
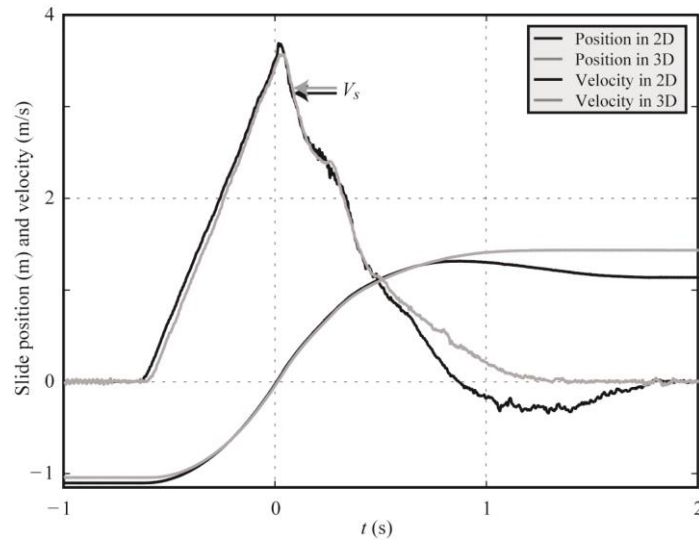
**Fig. 4.** Slide positions and velocities versus time for 2D and 3D tests with $\mathsf{F} \approx 2.05$, $S = 0.50$ and $M = 1.81$; the slide nose reaches the still water surface (position = 0) at time $t = 0$.
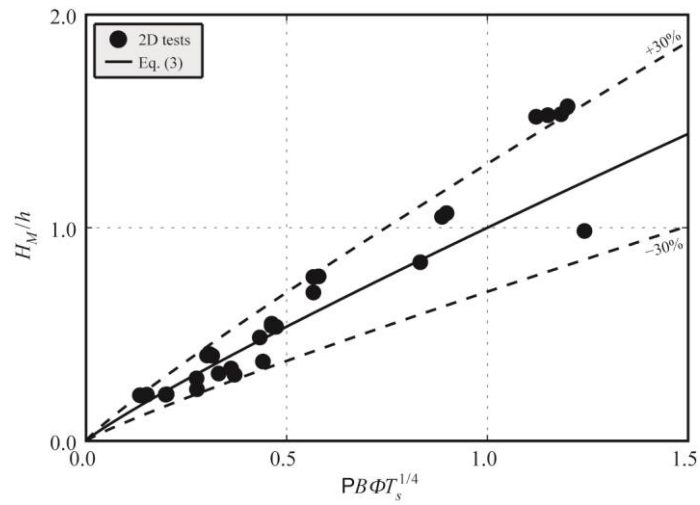


**Fig. 5.** Maximum relative wave height $H_M/h$ versus $\mathsf{P}B\Phi T_s^{1/4}$ with (-) Eq. (3) and (--) $\pm 30\%$ ($R^2 = 0.86$); the axes labels and Eq. (3) are taken from Heller and Spinneken (2013).

**Fig. 6.** Series of images of slide impact and tsunami generation in 3D for a test with $F = 1.15$, $S = 0.25$ and $M = 0.25$; the time interval from (b) onwards is 0.2 s.
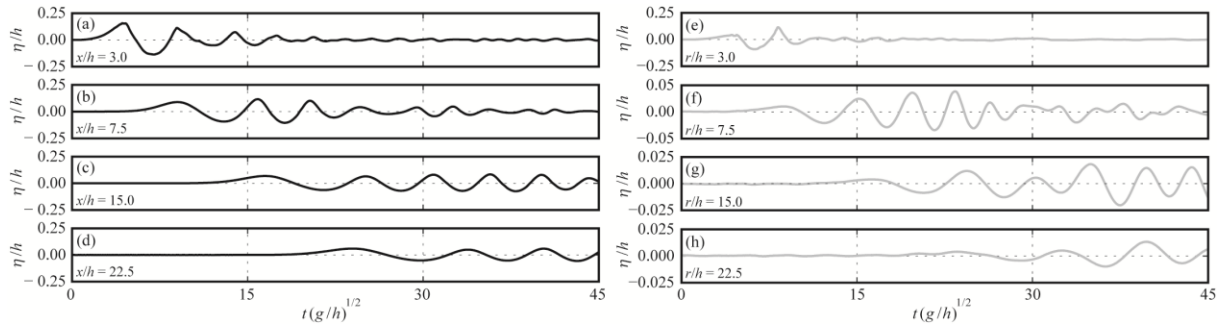
**Fig. 7.** Comparison of relative water surface elevations $\eta/h$ versus relative time $t(g/h)^{1/2}$ along the slide axis $\gamma = 0°$ for $\mathsf{F} \approx 1.10$, $S = 0.25$ and $M = 0.25$ in 2D at (a) $x/h = 3.0$, (b) 7.5, (c) 15.0, (d) 22.5 and in 3D at (e) $r/h = 3.0$, (f) 7.5, (g) 15.0 and (h) 22.5; note the increased scale on the ordinate in (f), (g) and (h).
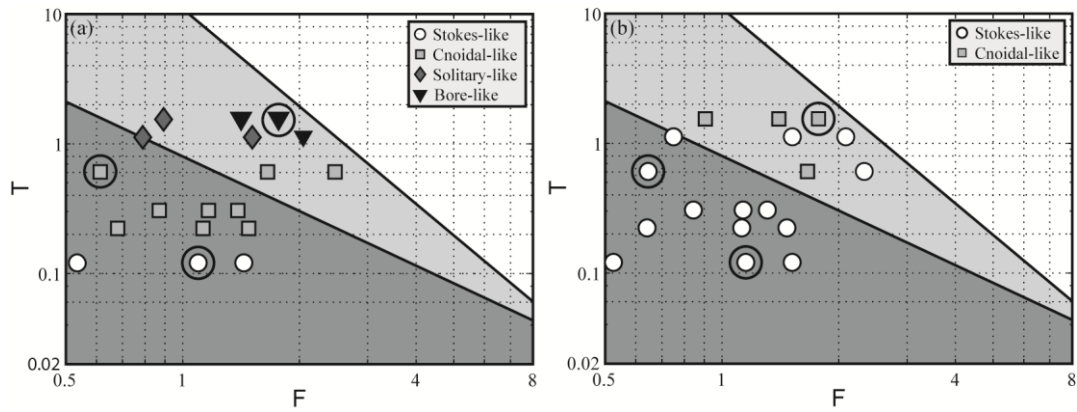


**Fig. 8.** Wave types of primary wave along the slide axis based upon the granular slide classification proposed by Heller and Hager (2011); (a) 2D and (b) corresponding 3D tests; the decay of the encircled tests are shown in Fig. 10.
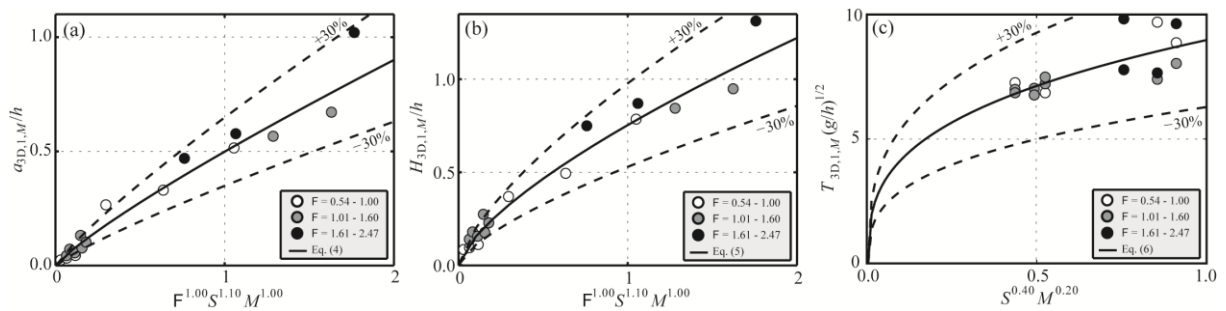
**Fig. 9.** Maximum 3D primary wave features: (a) maximum relative amplitude $a_{3D,1,M}/h$ versus $\mathsf{F}^{1.00}S^{1.10}M^{1.00}$ with (-) Eq. (4) and (--) $\pm30\%$ ($R^2 = 0.96$), (b) maximum relative height $H_{3D,1,M}/h$ versus $\mathsf{F}^{1.00}S^{1.10}M^{1.00}$ with (-) Eq. (5) and (--) $\pm30\%$ ($R^2 = 0.97$) and (c) corresponding maximum relative period $T_{3D,1,M}(g/h)^{1/2}$ versus (-) Eq. (6) with (--) $\pm30\%$ ($R^2 = 0.50$).
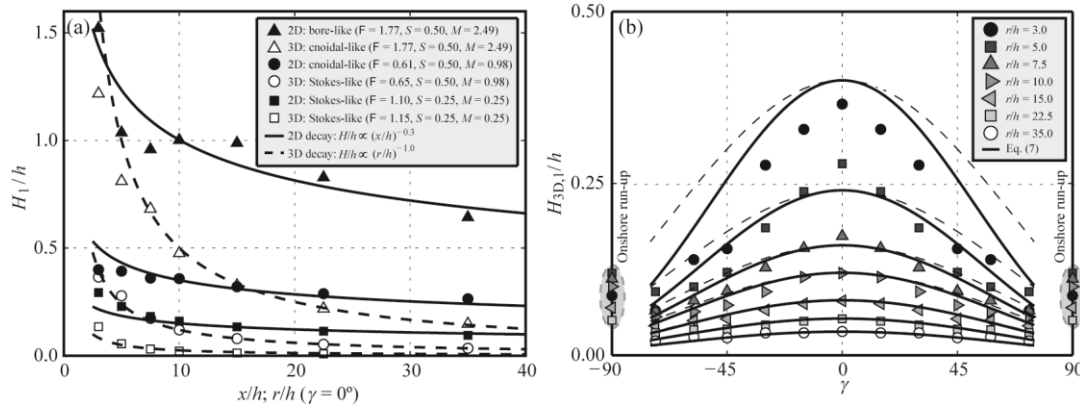


**Fig. 10.** 3D primary wave height decay: (a) wave height evolution along the slide axis for the three selected tests encircled in Fig. 8 including the corresponding 2D tests and (b) relative primary wave height decay $H_{3D,1}/h$ of a test with $\mathsf{F} = 0.65$, $S = 0.50$ and $M = 0.98$ as a function of $r/h$ and $\gamma$ fitted with (-) $(r/h)^{-1.0}f_\gamma$ after Eq. (7); the dashed lines shows Eq. (7) without the cosine exponent correction term $\{\{1 + \exp[-0.2(r/h)]\} = 1\}$; also included are the onshore wave run-up data at $\gamma = 90°$, which were correlated separately.
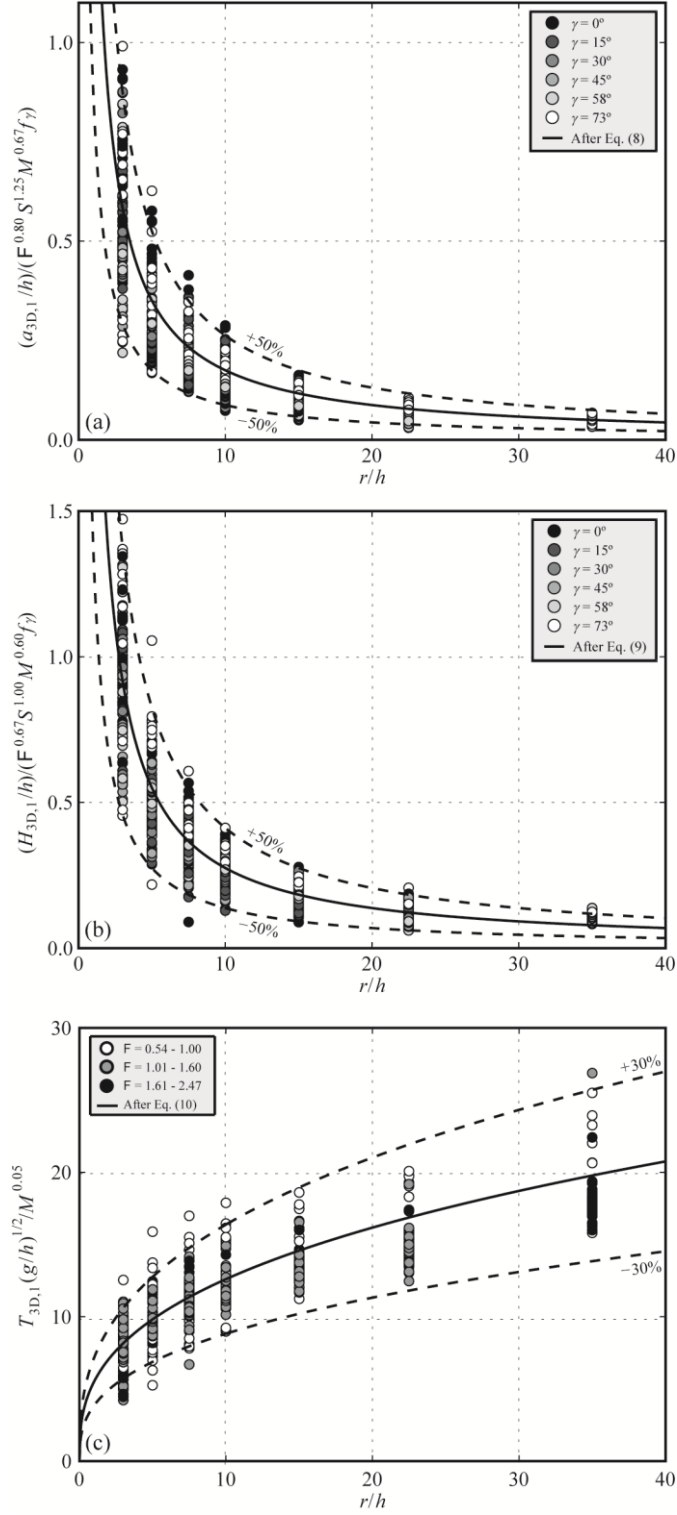
**Fig. 11.** Correlation of 3D data with (a) normalised primary wave amplitude $a_{3D,1}$ with (-) after Eq. (8) and (--) ±50% ($R^2 = 0.76$), (b) normalised primary wave height $H_{3D,1}$ with (-) after Eq. (9) and (--) ±50% ($R^2 = 0.83$) and (c) normalised primary wave period $T_{3D,1}$ with (-) after Eq. (10) and (--) ±30% ($R^2 = 0.70$).
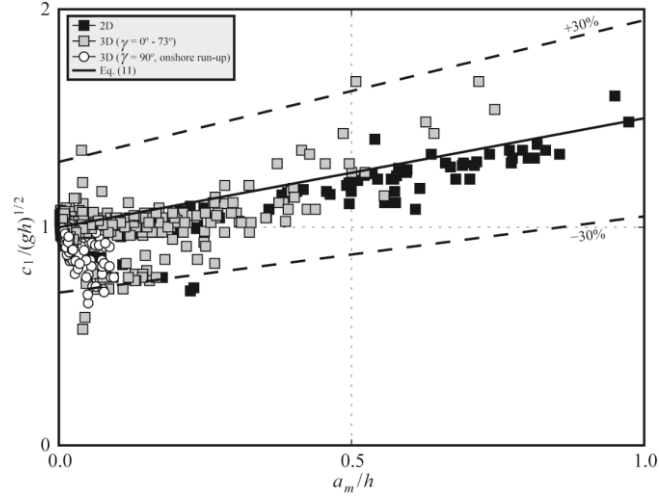
**Fig. 12.** Dimensionless primary wave celerity $c_1/(gh)^{1/2}$ versus mean wave amplitude $a_m/h$ between two subsequent wave probes of both 2D and 3D tests, including onshore wave run-up, with (-) Eq. (11) and (--) ±30%.
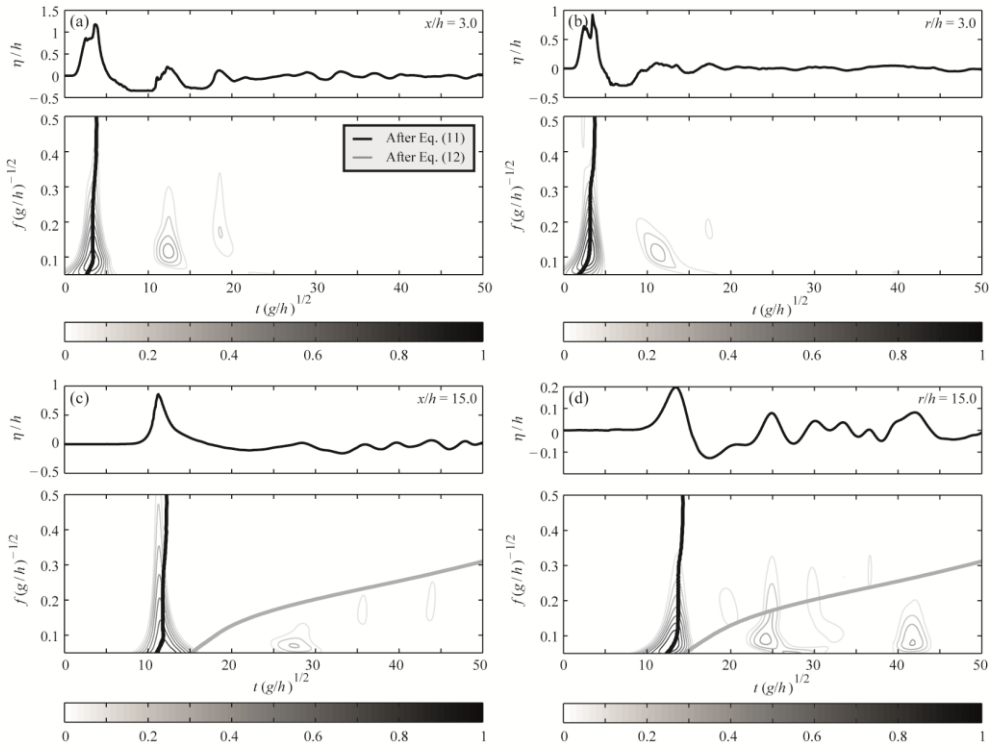


**Fig. 13.** Wavelet spectra of the up-most encircled bore-/cnoidal-like waves in Fig. 8 with $F$ = 1.77, $S$ = 0.50 and $M$ = 2.49 conducted in both 2D (a,c) and 3D (b,d) at $x/h = r/h$ = 3.0 and 15.0; further shown are the wave propagation celerity models after Eqn. (11) and (12).
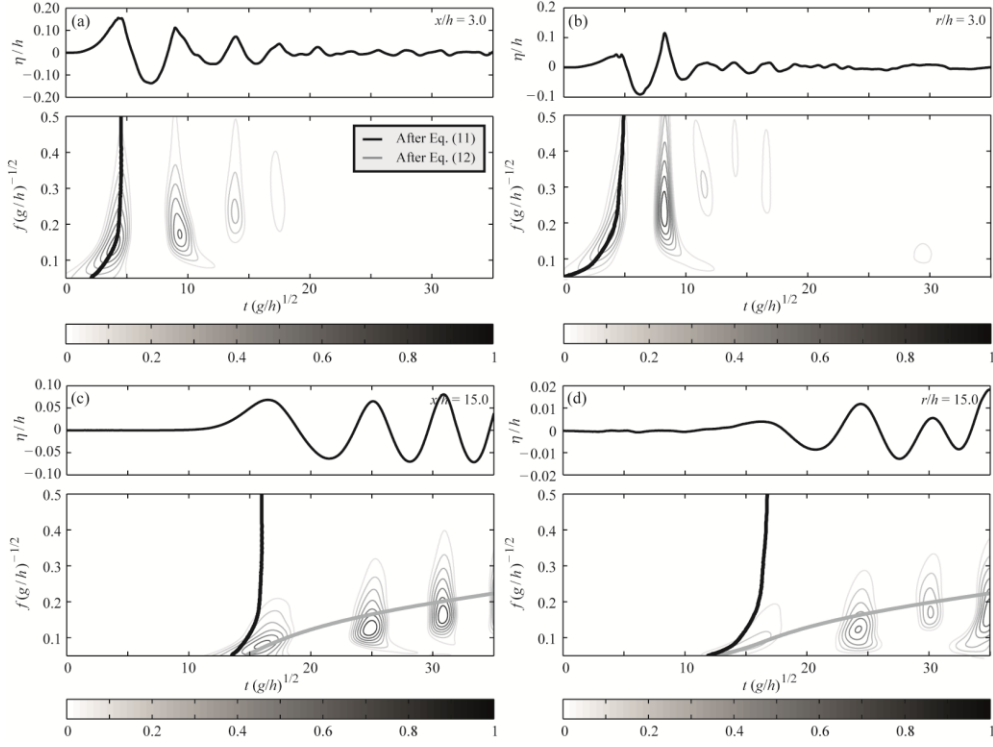
**Fig. 14.** Wavelet spectra of the lower-most encircled Stokes-like waves in Fig. 8 with $\mathsf{F} \approx$ 1.10, $S = 0.25$ and $M = 0.25$ conducted in both 2D (a,c) and 3D (b,d) at $x/h = r/h =$ 3.0 and 15.0; further shown are the wave propagation celerity models after Eqn. (11) and (12).
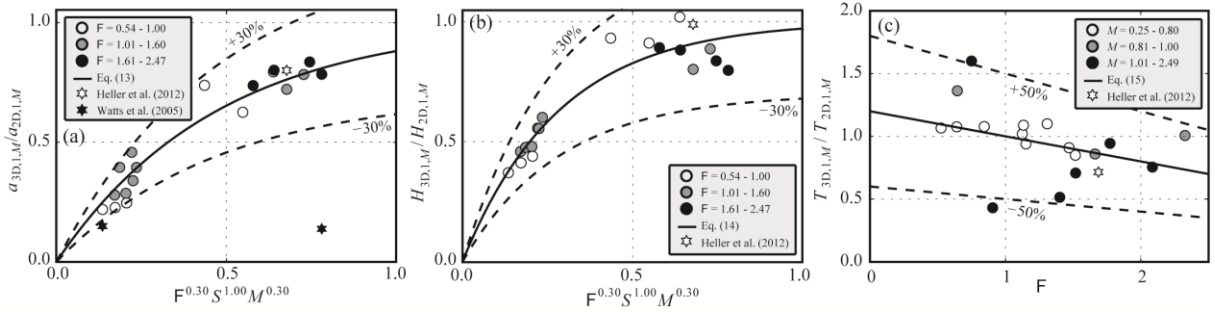


**Fig. 15.** 2D to 3D transformation of maximum primary wave parameters: (a) maximum primary wave amplitude ratios $a_{3D,1,M}/a_{2D,1,M}$ with (-) Eq. (13) and (--) $\pm 30\%$ ($R^2 =$ 0.93), (b) maximum primary wave height ratios $H_{3D,1,M}/H_{2D,1,M}$ with (-) Eq. (14) and (--) $\pm 30\%$ ($R^2 = 0.88$) and (c) maximum primary wave period ratios $T_{3D,1,M}/T_{2D,1,M}$ with (-) Eq. (15) and (--) $\pm 30\%$ ($R^2 = 0.16$).
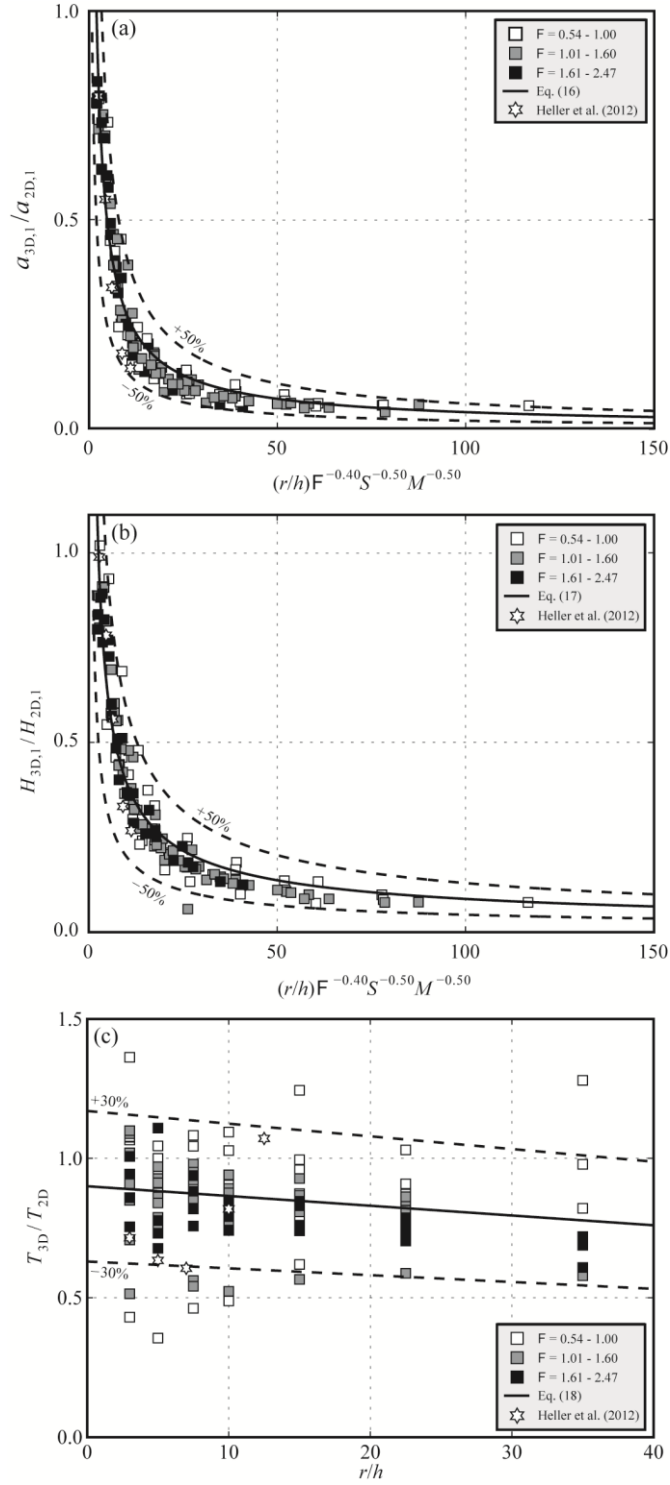
**Fig. 16.** Ratios of 3D to 2D primary wave parameters along slide axis: (a) wave amplitude ratios $a_{3D,1}/a_{2D,1}$ with (-) Eq. (16) and (--) $\pm 50\%$ ($R^2 = 0.92$), (b) wave height ratios $H_{3D,1}/H_{2D,1}$ with (-) Eq. (17) and (--) $\pm 50\%$ ($R^2 = 0.90$) and (c) wave period ratios $T_{3D,1}/T_{2D,1}$ with (-) Eq. (18) and (--) $\pm 50\%$ ($R^2 = 0.03$).
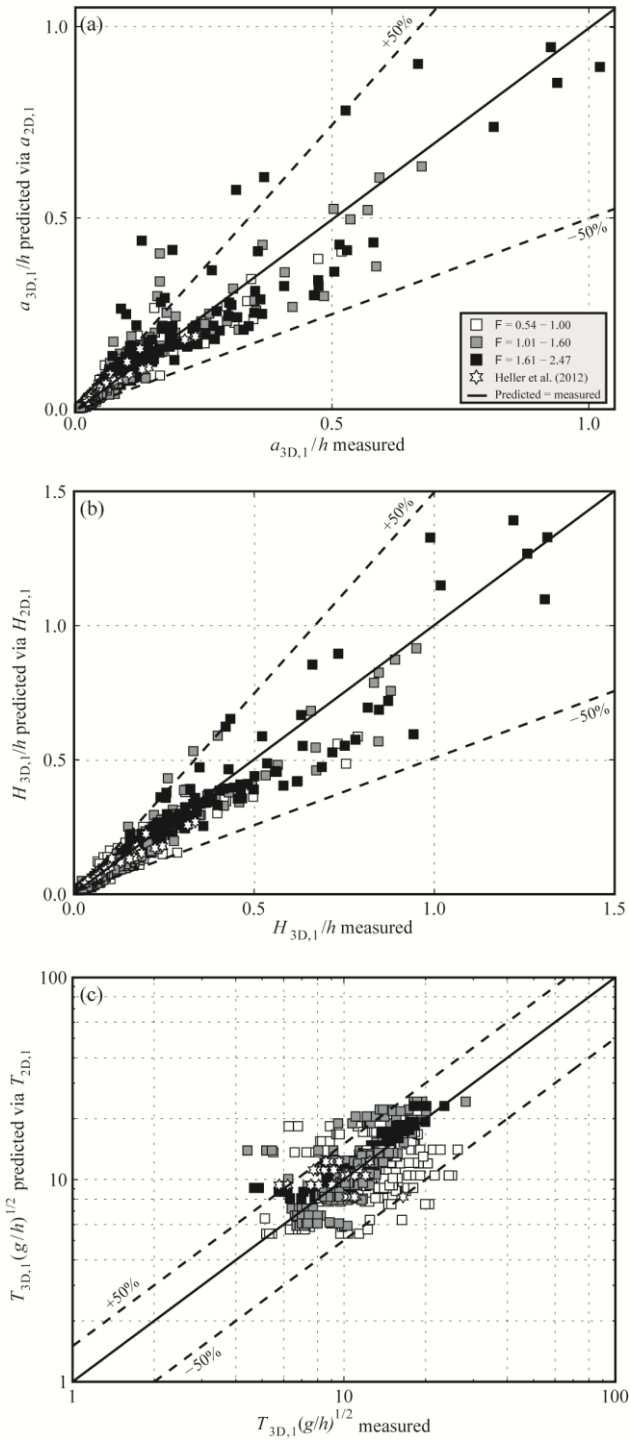
**Fig. 17.** 3D primary wave parameters predicted via 2D wave parameters versus measured wave parameters for (a) relative primary wave amplitude $a_{3D,1}/h$ with (-) Eq. (19) and (--) ±50% ($R^2 = 0.88$), (b) relative primary wave height $H_{3D,1}/h$ with (-) Eq. (20) and (--) ±50% ($R^2 = 0.92$) and (c) relative primary wave period $T_{3D,1}(g/h)^{1/2}$ with (-) Eq. (18) and (--) ±50% ($R^2 = 0.33$).
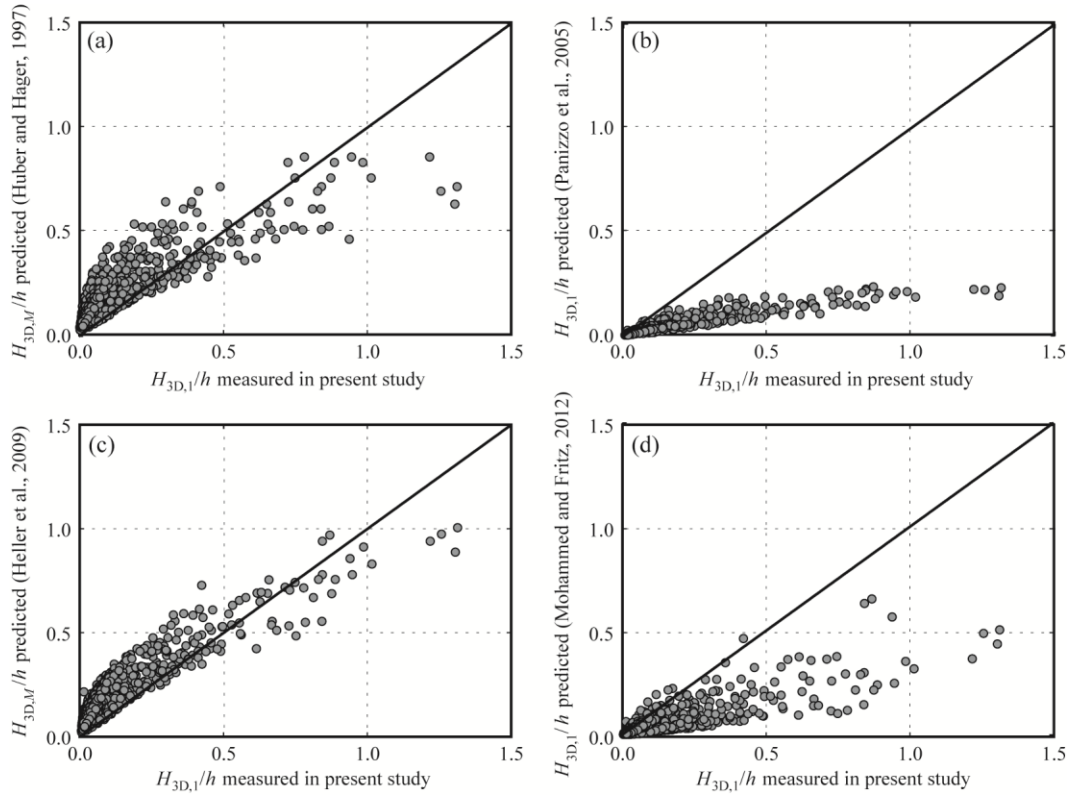
**Fig. 18.** Comparison of 3D measured relative primary wave height $H_{3D,1}/h$ of present study with prediction with empirical equation of (a) Huber and Hager (1997) [Eq. (21) for maximum wave and granular slides], (b) Panizzo et al. (2005) [Eq. (22) for primary wave and solid slides], (c) Heller et al. (2009) [Eq. (23) for maximum wave and granular slides] and (d) Mohammed and Fritz (2012) [Eq. (24) for primary wave and granular slides].
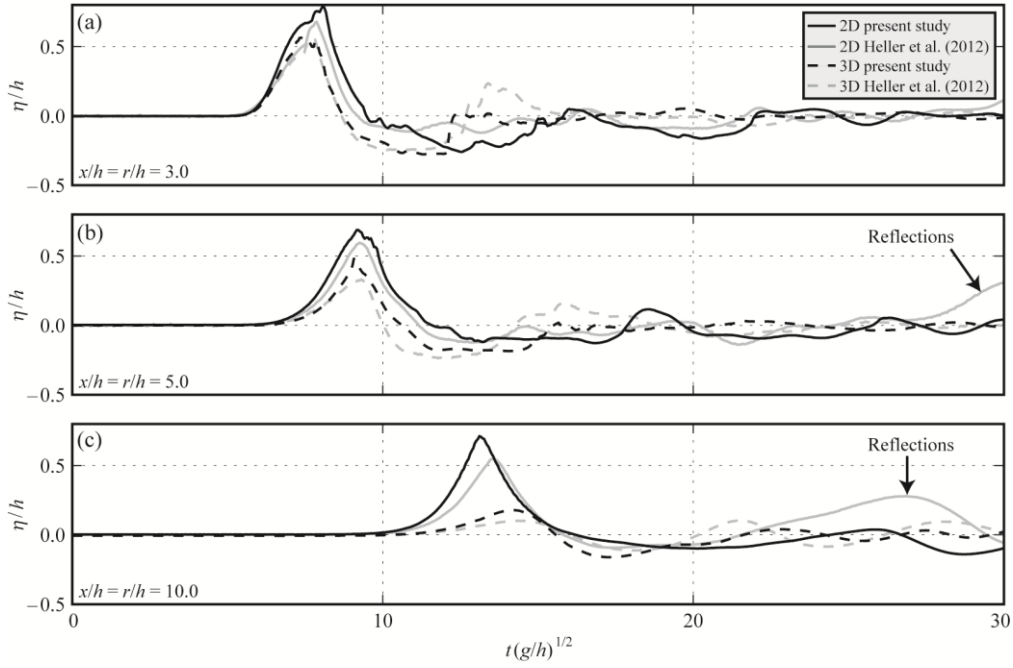
**Fig. 19.** Scale effects: comparison of 2D and 3D relative water surface elevations of a test of the present study ($F = 1.51$, $S = 0.50$ and $M = 1.81$) with a similar test ($F \approx 1.71$, $S = 0.50$ and $M = 1.65$) conducted in the small scale study of Heller et al. (2012); the profiles are shown at (a) $x/h = r/h = 3.0$, (b) 5.0 and (c) 10.0.
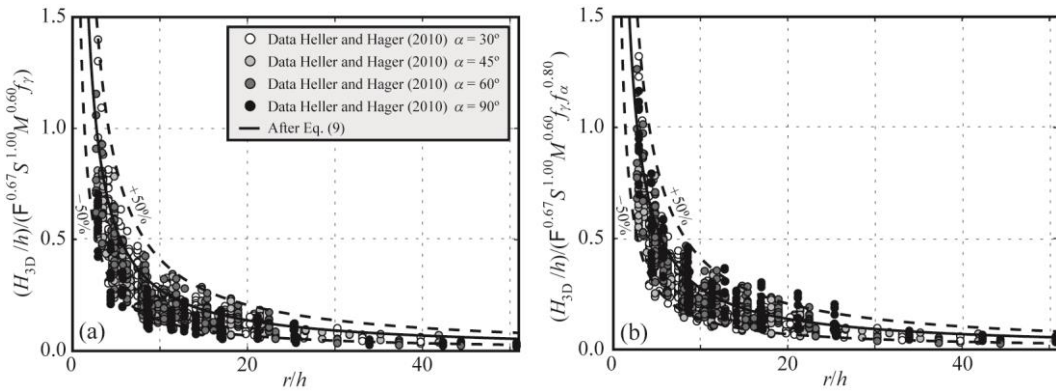


**Fig. 20.** Validation of 2D to 3D transformation method with 2D data of Heller and Hager (2010): (a) normalised transformed relative wave height $H_{3D}/h$ with (-) after Eq. (9) and (--) ±50% ($R^2 = 0.58$) and (b) improved fit with normalised relative wave height $H_{3D}/h$ divided by slide impact angle correction term $f_\alpha^{0.80}$ with (-) after Eq. (9) and (--) ±50% ($R^2 = 0.71$).
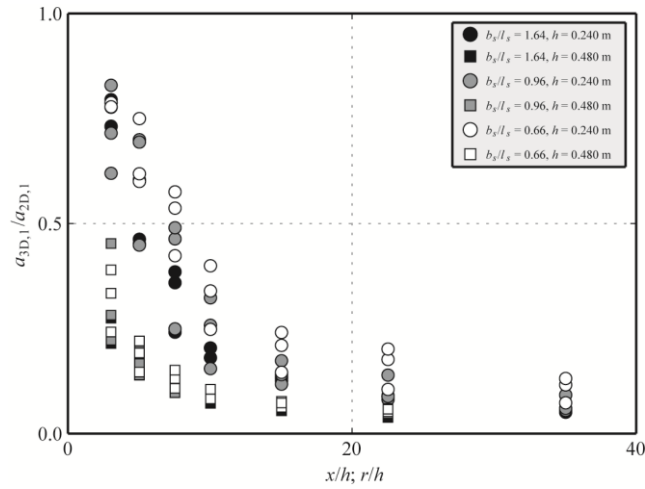
**Fig. A.1.** Illustration of effect of slide width to length ratio $b_s/l_s$ on the wave amplitude ratios $a_{3D,1}/a_{2D,1}$ along the slide axis.
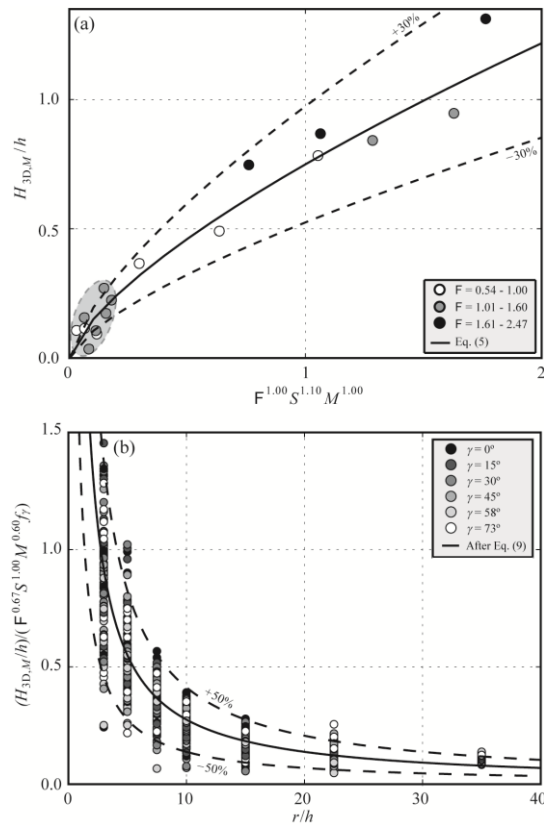


**Fig. B.1.** Maximum relative wave heights correlated with the same expressions as the primary wave heights: (a) maximum relative wave height $H_M/h$ versus $F^{1.00}S^{1.10}M^{1.00}$ with Eq. (5) and (--) $\pm 30\%$ ($R^2 = 0.96$) and (b) normalised maximum wave height $H_{3D,M}/h$ with (-) after Eq. (9) and (--) $\pm 50\%$ ($R^2 = 0.78$).
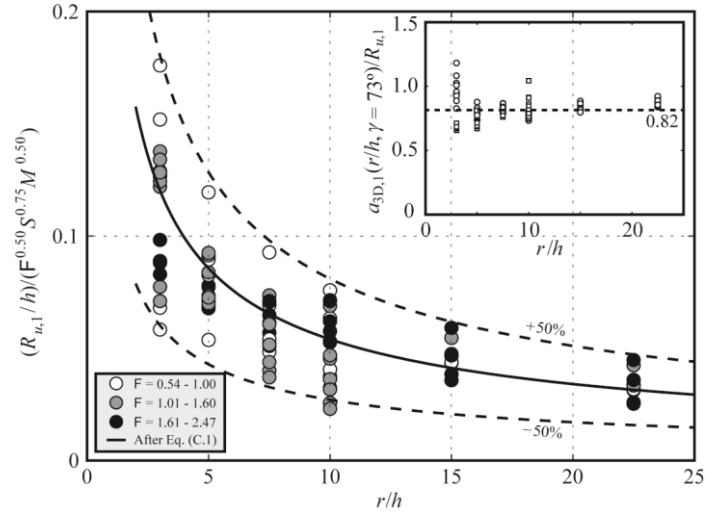
**Fig. C.1.** Relative primary onshore wave run-up $R_{u,1}/h$ over $\mathsf{F}^{0.50}S^{0.75}M^{0.50}$ versus relative radial distance $r/h$ with (-) after Eq. (C.1) and (--) $\pm 50\%$ ($R^2 = 0.62$); inset: linkage of off- and onshore waves of primary 3D wave amplitude relative to primary onshore wave run-up $a_{3D,1}(r/h, \gamma = 73°)/R_{u,1}$ versus $r/h$, with a mean of 0.82.
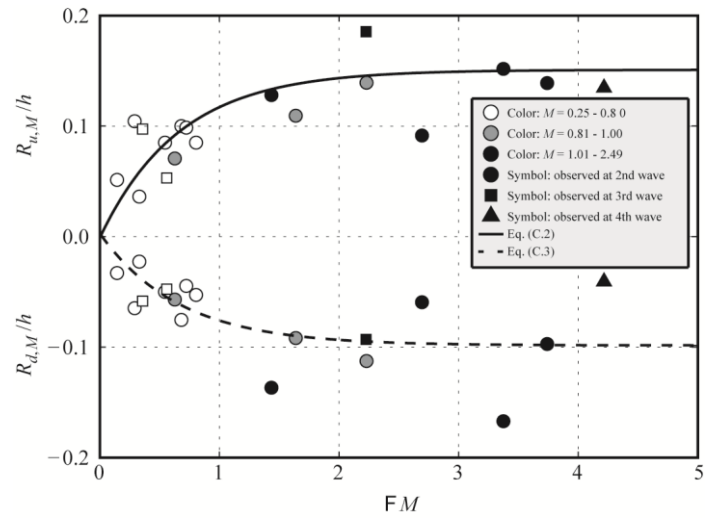


**Fig. C.2.** Maximum relative onshore wave run-up $R_{u,M}/h$ and run-down $R_{d,M}/h$ versus $\mathsf{F}M$ with (-) Eq. (C.2) ($R^2 = 0.49$) and (--) Eq. (C.3) ($R^2 = 0.38$).
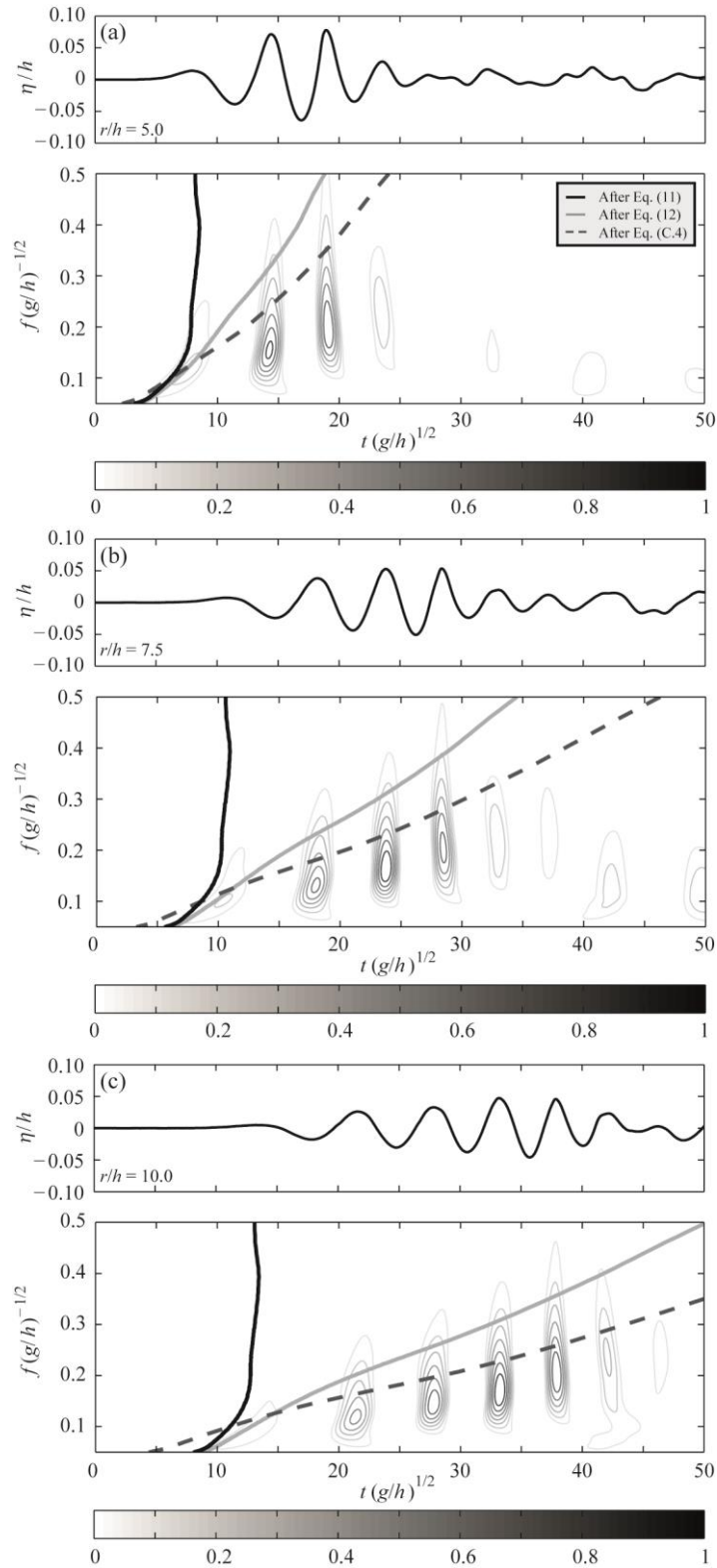
**Fig. C.3.** Wavelet spectra of onshore waves of the lower-most encircled Stokes-like waves in Fig. 8 with $F \approx 1.10$, $S = 0.25$ and $M = 0.25$ at (a) $r/h = 5.0$, (b) 7.5 and (c) 10.0; further shown are the wave propagation celerity models after Eqn. (11), (12) and (C.4).